On the large-scale structures in two-dimensional, small-deficit, turbulent wakes

By I. WYGNANSKI, F. CHAMPAGNE AND B. MARASLI

Aerospace and Mechanical Engineering Department, University of Arizona,
Tucson, AZ 85721, USA.

A systematic study of two-dimensional, turbulent, small-deficit wakes was carried out to determine their structure and the universality of their self-preserving states. Various wake generators, including circular cylinders, a symmetrical airfoil, a flat plate, and an assortment of screens of varying solidity, were studied for a wide range of downstream distances. Most of the generators were tailored so that their drag coefficients, and therefore their momentum thicknesses, were identical, permitting comparison at identical Reynolds numbers and aspect ratios. The flat plate and airfoil had a small, trailing-edge flap which could be externally driven to introduce forced sinuous oscillations into the wake. The results indicate that the normalized characteristic velocity and length scales depend on the initial conditions, while the shape of the normalized mean velocity profile is independent of these conditions or the nature of the generator. The normalized distributions of the longitudinal turbulence intensity, however, are dependent on the initial conditions.

Linear inviscid stability theory, in which the divergence of the mean flow is taken into account, predicts quite well the amplification and the transverse distributions of amplitudes and phases of externally imposed sinuous waves on a fully developed turbulent wake generated by a flat plate. There is a strong indication that the large structures observed in the unforced wake are related to the two-dimensional instability modes and therefore can be modelled by linear stability theory. Furthermore, the interaction of the two possible modes of instability may be responsible for the vortex street-type pattern observed visually in the small-deficit, turbulent wake.

1. Introduction

Turbulent, plane wakes generated by circular cylinders in the absence of a pressure gradient have been the subject of numerous experimental investigations, the most notable of which are those by Townsend (1947, 1949). The results of these studies, along with results obtained in other free shear flows, led to the early ideas of self-preservation and Reynolds number independence proposed by Townsend (1956). It was postulated that, sufficiently far downstream from the cylinder, an asymptotic self-preserving state is achieved for which the flow can be described by a single velocity scale u_0 and a single lengthscale L_0 (see figure 1). That is, the transverse distributions of mean velocity and Reynolds stress must be independent of the streamwise coordinate x when normalized by these scales. One question under investigation presently is to determine whether and where these scales can be considered unique.

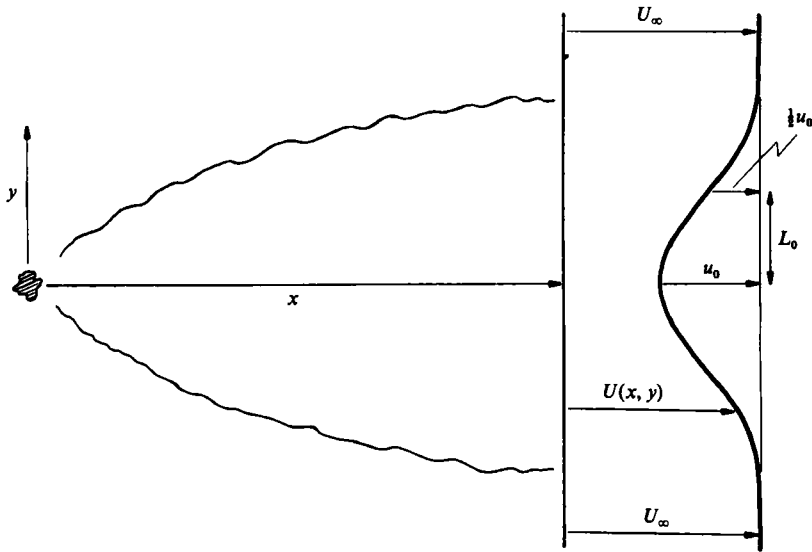It has been well established (Townsend 1956; Uberoi & Freymuth 1969; Symes &

FIGURE 1. A sketch defining the nomenclature.

Fink 1977; Yamada *et al.* 1980) that far-awake flows are self-preserving and that the velocity and length scales, u_0 and L_0, vary as $(x-x_0)^{-\frac{1}{2}}$ and $(x-x_0)^{\frac{1}{2}}$, respectively, as predicted by the equations of motion and the momentum integral constraint. The virtual origin, x_0, is used to account for viscous or Reynolds-number effects. Furthermore, Townsend (1956) indicated that at sufficiently high Reynolds number, L_0/d and u_0/U_∞ are universal functions of x/d only, where d is the diameter of the cylinder. The initial motivation for the present study stemmed from comparing some early measurements describing the downstream variation of the streamwise component of turbulence intensity. We observed large differences between our data and data reported in the literature that could not be attributed to experimental technique (figure 2). Large differences between the various results are evident, and the trends in the data are quite different at large $x/C_D\,d$, where C_D is the drag coefficient. At the time (*circa* 1970), most investigators used the cylinder diameter for the purpose of normalization. Considerations based on the equations of motion show that the momentum thickness, θ, should have been used as the normalizing lengthscale for the small-deficit wake. That is, the drag force exerted on the fluid by the cylinder should be used to define the initial flow conditions. We will use 2θ because $C_D\,d = 2\theta$. It can be shown that the normalized velocity and length scales should vary as

$$\left(\frac{U_\infty}{u_0}\right)^2 \sim \left(\frac{x-x_0}{2\theta}\right), \quad \left(\frac{L_0}{\theta}\right)^2 \sim \left(\frac{x-x_0}{2\theta}\right). \tag{1.1}$$

The data of Townsend (1956), Symes & Fink (1977), and Yamada *et al.* (1980) confirm the above relations and show that mean velocity profiles observed by each investigator are self-similar when scaled by their individual velocity and length scales. However, comparison of the data indicates a possible lack of universality in the behaviour of these scales; that is, different wakes developed differently with downstream distance.

Sreenivasan (1981) examined the manner in which wakes produced by a variety of generators approached self-preserving states. He observed substantial differences
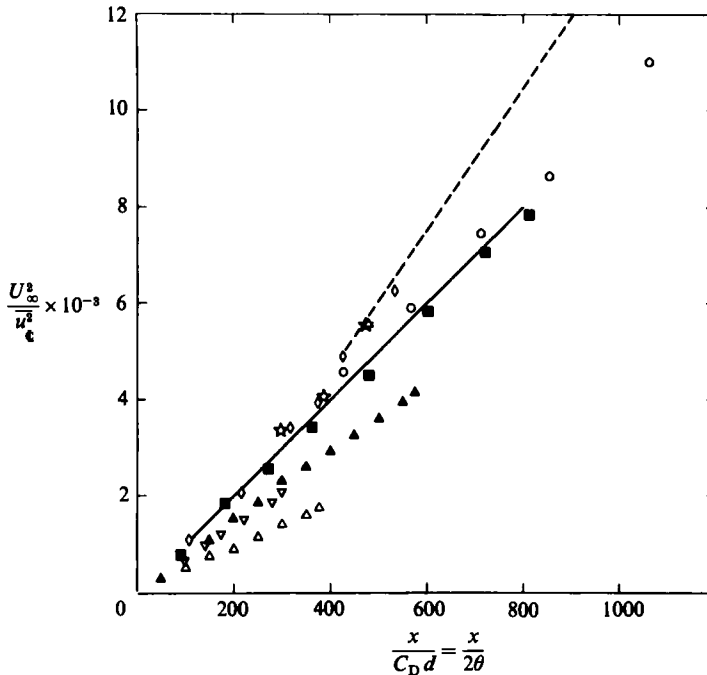
FIGURE 2. Centreline turbulence intensity for wakes generated by circular cylinders. $\bigcirc$, Marasli (1983), $Re = 1360$, AR $= 384$; $\blacksquare$, Marasli, $Re = 5900$, AR $= 128$; $\diamondsuit$, Townsend (1956), $Re = 1360$, AR $= 240$; - - -, Townsend (1949); ———, Uberoi & Freymuth (1969), $Re = 4320$, AR $= 192$; $\star$, Yamada *et al.* (1980), $Re = 4000$, AR $= 80$; $\triangledown$, Champagne (1978), $Re = 19000$, AR $= 32$; $\blacktriangle$, Symes & Fink (1977), $Re = 6666$, AR $= 150$, no ext. turb. added; $\triangle$, Symes & Fink, with ext. turb. added.

in the way these flows evolved, even though each flow preserved the shape of the mean velocity profile when normalized by its own characteristic scales. Sreenivasan & Narasimha (1982) suggested that a unique self-preserving state exists for all plane wakes and defined the characteristic constants stemming from their suggestion. We felt at the time that their data did not fully support their conclusion, and the present study compiles further evidence negating it.

A possible explanation for the lack of uniqueness is suggested by the results of Symes & Fink (1977), who investigated the effect of free-stream turbulence on the development of wakes. They showed that the relative scale of the external turbulence, rather than the level of the turbulence intensity, was an important parameter affecting the development of the wake. As each experimental facility has its own characteristic free-stream disturbances, wakes generated in a particular facility may be unique to that facility only. The lack of universality of various small-deficit wake flows might be explained in terms of the instability of the mean velocity profile in the wake. Related to this are the flow visualization results of Cimbala, Nagib & Roshko (1981), which revealed that large coherent structures develop far downstream from the wake generator and these are not necessarily related to the vortices shed from the generator. This was sufficient evidence to suggest that the wake, like the mixing layer, contains large-scale coherent structures which may have a wave-like behaviour. Travelling, large structures were observed in both laminar (Freymuth 1966) and turbulent (Brown & Roshko 1974; Oster & Wygnanski 1982) mixing layers, and their behaviour was explained by an instability mechanism (Michalke 1965;

Gaster, Kit & Wygnanski 1985). The similarity of the patterns occurring in both laminar and turbulent states is not surprising in view of the fact that the instability mechanism is principally inviscid and is controlled by the mean velocity profiles, which are similar in both situations. Gaster *et al.* computed the amplitude distributions and the phase speeds of travelling waves associated with large coherent structures in the plane turbulent mixing layer, and they obtained very good agreement with experimental results by accounting for the effects of mean flow divergence. The mean velocity profile in the wake is also inviscidly unstable, and its shape is not affected by transition from laminar to turbulent flow, suggesting that a similar analysis could predict the evolution of the large-scale structures in this flow as well.

The stability and transition of a plane wake, generated by a thin plate placed parallel to a uniform flow, was considered by many investigators (e.g. Sato & Kuriki 1961; Mattingly & Criminale 1972; Zabuski & Deem 1971). The analysis in these investigations was always concerned with the immediate neighbourhood of the trailing edge, where the velocity deficit was greater than 60% of the free-stream velocity. Sato & Kuriki (1961) limited their analysis to a temporal evolution of the instability at one location in the flow, and Mattingly & Criminale (1972) considered the instability of the wake to natural disturbances in both time and space and concluded that the spatial evolution of a travelling wave gives superior predictions for the disturbance characteristics experimentally observed. The analysis invariably assumed that the flow was parallel and was therefore limited to a prescribed streamwise location in which the width of the wake was defined. The parallel flow assumption represents a severe constraint on predicting growing disturbances in the wake because, in addition to the local width of the flow, the characteristic velocity scale must also change as a result of the divergence.

In contradistinction to the mixing layer, the plane wake is susceptible to both symmetrical (varicose) and antisymmetrical (sinuous) modes of instability. The varicose mode was traditionally disregarded (e.g. Sato & Kuriki 1961) because calculations based on the parallel flow approximations indicated that the most strongly amplified disturbances were sinuous. Data obtained in this investigation attribute the lack of universality of the self-preserving wake, at least partially, to the interaction between the two modes. Certainly, if one is interested in examining the wake over long distances, one cannot neglect the varicose mode of instability.

The scope of the present investigation is limited to the small-deficit wake starting some 100 momentum thicknesses from the generator and extending to 2000 momentum thicknesses downstream. The flow was always incompressible, with free-stream velocities not exceeding 35 m/s and typical Reynolds numbers of a few thousand.

2. Experimental Arrangement

The wakes were generated in the University of Arizona wind tunnel facility. The 80-ft-long tunnel is a closed-circuit type built by Kenney Engineering of California and is nearly identical to its counterparts at Tel Aviv University and the University of Southern California. The test section is 2 ft wide, 3 ft high, and 20 ft long. The top and bottom walls, which are adjustable in height, were adjusted to compensate for boundary-layer growth and to obtain a zero streamwise pressure gradient. A 30 hp, variable-speed motor with tachometer generator and a motor controller drives an axial flow fan with variable-pitch blades. The blades were set to their minimum pitch angle to minimize large-scale turbulence generation. In this configuration, the fan

easily supplied the necessary range of speeds in the test section required for the present study, that is, 2 to 35 m/s. The tunnel is equipped with chilled water cooling coils just downstream of the diffuser section and an electric heating unit just upstream of the fan to control the flow temperature. A Minco platinum resistance thermometer, connected to a special bridge and digital panel display unit, allows measurement of the mean temperature of the flow to ± 0.05 °C.

The plenum chamber contains 4-inch-thick hexcell honeycomb, five 20-mesh stainless-steel screens, and a 4-ft stilling section. Following this section is the 10:1 contraction section with a fifth-order polynomial contour to ensure separation-free acceleration of the flow to the test section. The wake generators were mounted horizontally across the 2-foot span of the test section at a streamwise location 2 feet downstream from the inlet. Measurements of the velocity profile at this plane indicated that the flow was uniform to ± 0.25 %. The free-stream disturbance level in the streamwise velocity component is approximately 0.03 %. The free-stream speed was monitored using a pitot tube placed 1 foot below the wake generator and about 2 inches into the flow. The Pitot tube was connected to an MKS Baratron pressure transducer unit.

Velocities were measured using a rake of nine Disa 55P01 hot-wire probes connected to Disa 55M01 and 56C01 constant temperature anemometers. The rake, which was 1.75 inches in total height, was used to measure the mean streamwise component of the instantaneous velocity. The rake was mounted on an internal traversing mechanism with a swept-forward, thin extension arm, placing the probes upstream of any region of flow interference caused by the mechanism. The mechanism permitted traversing in the streamwise and vertical directions with resolutions of 0.10 and 0.01 inch, respectively. The anemometer signals were conditioned using buck and gain amplifiers and simple low pass RC filters with a 6-dB cutoff point at 10 kHz. The conditioned signals were sent directly to the analog-to-digital converter in the data acquisition system. An LSl 11/23 data acquisition/on-line computer system was used for digital signal processing. The major components of the system include an LSl 11/23 microprocessor, a 15-bit A/D converter with 10 channels of simultaneous sample-and-hold circuitry; a dual-density, 125-ips, tape drive; a 160 M-byte hard disk; 256 K-byte static memory; a printer/plotter; two Tektronix 4006 graphic terminals; a Tektronix 4611 hard-copy unit; and a SKYMNK array processor. The multiple channel capability allows simultaneous, continuous sampling of up to 10 channels, with variable sampling frequency up to 10 kHz. The system can be used as a data logger, i.e. to create digital tapes, or as an on-line computer for real-time analysis.

For calibration, the hot wires were placed in the free stream, well outside the wake, along with a Pitot tube which was mounted near the rake. The bridge voltage signals and the output of the pressure transducer connected to the Pitot tube were sent to the A/D converter. An nth-order polynomial, $U = P_n(E)$, where the independent variable E is the conditioned bridge voltage, was fit to several calibration velocities for each hot wire, thereby providing an overall calibration for each sensor. The wires were calibrated only over the range of velocities to be measured in the wake, typically $0.80\ U_\infty$ to $1.05\ U_\infty$. Whenever the velocity deficits exceeded $0.20\ U_\infty$, a second-order polynomial was used; whereas for $u_0 < 0.10\ U_\infty$, a linear fit was adopted, speeding on-line computations.

During the course of the experiments, the temperature of the flow was maintained at ± 0.10 °C of the calibration temperature. The hot wires were continuously checked
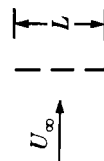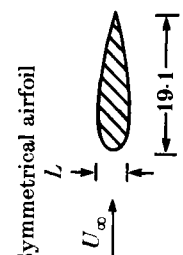
Wake generators	$L \times$ width (mm)	$\dfrac{U_\infty L}{\nu}$	$\dfrac{U_\infty \theta}{\nu}$	θ (mm)	Remarks	
Circular cylinders						
	1.59 × 610	1360, 2000, 3000	640, 925, 1410	0.74	$l/d = 384$ Drill rod	
	4.76 × 610	2000, 4000, 5800	933, 1990, 3200	2.23, 2.33, 2.64	$l/d = 128$ Drill rod	
	6.35 × 610	5800	3220	2.64	$l/d = 96$ Drill rod	
Screens & solid strip					Solidity	Mesh
	8.89 × 610	—	1980	2.32	30%	28 × 28
	6.60 × 610	—	2010	2.33	45%	40 × 40
	4.57 × 610	—	2040	2.39	70%	50 × 50
	2.54 × 610	2166	1970	2.31	100%	—
Flat plate						
	6.35 × 610	2780	1035	2.36	Rounded leading edge; tapered to 1 mm. Boundary layer on both sides tripped. Solid aluminum plate	
Symmetrical airfoil						
	7.62 × 610	6500	1996	2.34	Boundary layer tripped. Extruded aluminum tubing filled with sand	

TABLE 1. Summary of wake generators

for drift. The results were sensitive to any minor calibration changes because the maximum velocity deficit was of the order of 5 %. Generally, 27–36 data points were taken to define a mean velocity and turbulence intensity profile.

Lateral velocity component fluctuations were measured with a four-probe array of symmetric X-wires. The X-wires were calibrated in the free-stream portion of the wind tunnel using an anemometer response equation of the form

$$U - A_{3,j} \dot{V} = P_j(E_j) \quad (j = 1, 2),$$ (2.1)

where U and V are the calibration velocity components, E_j is the anemometer bridge voltage, and P_j is a second-order polynomial given by

$$P_j(E_j) = \sum_{n=0}^{2} A_{nj} E_j{}^n.$$ (2.2)

The X-wires were calibrated at 20 points (4 velocities and 5 yaw angles in the range $\pm 10°$) and the unknown constants A_{nj}, $n = 0, \ldots, 3$ and $j = 1, 2$, were solved by least-squares fit. The instantaneous velocity components U and V could then be computed from

$$V(t) = \frac{P_1(E_1) - P_2(E_2)}{A_{3,2} A_{3,1}}, \quad U(t) = P_1(E_1) - A_{3,1} V.$$ (2.3)

Again, the wires were calibrated only over the range of velocities to be measured in the wake.

The wake generators used in the present experiments are described in table 1. The circular cylinders were steel, drill rods and the screens and solid strip were stainless steel. The cylinder, screens, and solid strip were all mounted under adequate tension to ensure that the generators were straight and rigid. The screens and solid strip were specially constructed to have the same momentum thickness as the $\frac{3}{16}$-inch-diameter (4.76 mm) cylinder at $Re_d = 4000$. The aspect ratio $\mathscr{L}/d$ was approximately 240 for the referred cases. To introduce controlled excitations into the wake, a small flap (5 mm in length) was attached to the trailing edge of the flat plate and airfoil. Violin strings were used to connect the downstream edge of each side of the flap to two matched loudspeakers, one located on each side of the plate just outside the tunnel sidewalls. The speakers were driven in phase at the desired amplitudes and frequencies by an audio amplifier fed by a Krohn Hite function generator. The forcing frequency and amplitude were monitored by a frequency counter and r.m.s. meter.

3. Theoretical considerations

3.1. *Similarity conditions*

For a developing wake flow sufficiently far from the generator, the transverse distributions of mean velocity and Reynolds stresses are assumed to be self-preserving. That is, these distributions assume functional forms which are independent of x when normalized by the velocity and length scales, u_0 and L_0 respectively. This can be expressed in the form

$$\left. \begin{aligned} U &= U_\infty - u_0 f(\eta), \\ \overline{u^2} &= u_0^2 g_{11}(\eta), \\ \overline{uv} &= u_0^2 g_{12}(\eta), \\ \overline{v^2} &= u_0^2 g_{22}(\eta), \\ \overline{w^2} &= u_0^2 g_{33}(\eta), \end{aligned} \right\}$$ (3.1)

where $\eta = y/L_0$ and u_0 and L_0 are defined in figure 1. In general, u_0 and L_0 will be functions of the following parameters:

$$u_0, L_0 = \text{fcns}\,(x, \rho, u, U_\infty, F, \mathcal{L}, d, \text{geo}, u'_{\text{FS}}, N_{\text{FS}}, \text{others}) \tag{3.2}$$

where

$\mathcal{L}$ = span of the wake generator,

d = characteristic width of the wake generator,

geo = geometry of the wake generator,

u'_{FS} = amplitude of the free-stream disturbance level,

N_{FS} = nature of the free-stream disturbance,

F = drag force on the wake generator per unit length,

others = magnitude and nature of any vibration of the wake generator.

The conditions under which self-preserving flow is possible can be obtained by substituting the self-preserving distributions into the equations of mean momentum and turbulent kinetic energy and examining the coefficients in the resulting equations. For the small-deficit far wake in the absence of a pressure gradient, i.e. when $u_0/U_\infty \ll 1$, Townsend (1970) obtains the conditions

$$\frac{U_\infty L_0}{u_0^2}\frac{\mathrm{d}u_0}{\mathrm{d}x} \propto \frac{U_\infty}{u_0}\frac{\mathrm{d}L_0}{\mathrm{d}x}. \tag{3.3}$$

The self-preserving functions are also subject to the momentum integral constraint

$$\frac{F}{\rho U_\infty^2} = \int_{-\infty}^{\infty} \frac{U}{U_\infty}\left(1 - \frac{U}{U_\infty}\right)\mathrm{d}y = \theta, \tag{3.4}$$

where θ is the momentum thickness. In terms of the self-preserving function, f, this becomes

$$\frac{F}{\rho U_\infty^2 \theta} = \frac{u_0 L_0}{U_\infty \theta}\mathcal{I}_1 - \frac{u_0^2 L_0}{U_\infty^2 \theta}\mathcal{I}_2, \tag{3.5}$$

where

$$\mathcal{I}_n = \int_{-\infty}^{\infty} f^n(\eta)\,\mathrm{d}\eta \quad (n = 1, 2), \tag{3.6}$$

are constants for a given wake flow. However, (3.4)–(3.6) are only consistent with (3.3) when $u_0/U_\infty \ll 1$ and the second term in (3.5) is dropped. This places a constraint on the product $(u_0 L_0)$ of the two scales, since in the absence of a pressure gradient, F, θ, and U_∞ are constants independent of x. Dimensional reasoning, along with the linear part of (3.5), indicates the variables, F, ρ, and U_∞ in equation (3.2) should appear in the combination $F/\rho U_\infty$ [see also (3.4)]. It can be easily shown from (3.3) and (3.4) that

$$\frac{u_0}{U_\infty} \sim \left[\frac{F}{\rho U_\infty^2 (x - x_0)}\right]^{\frac{1}{2}} \sim \left[\frac{\theta}{x - x_0}\right]^{\frac{1}{2}}, \tag{3.7}$$

and

$$L_0 \sim \left[\frac{F(x - x_0)}{\rho U_\infty^2}\right]^{\frac{1}{2}} \sim [\theta(x - x_0)]^{\frac{1}{2}}, \tag{3.8}$$

where x_0, the virtual origin, is commonly assumed to depend on the Reynolds number and geometry of the generator. This indicates that θ is the appropriate normalizing length scale.

If a universal self-preserving state exists independent of initial conditions, free-stream disturbances, and other parameters, the normalized distribution functions f

and gs are universal functions and u_0 and L_0, the normalized velocity and length scales, should vary as

$$\left(\frac{U_\infty}{u_0}\right)^2 = A\bar{x},\tag{3.9}$$

and

$$\left(\frac{L_0}{\theta}\right)^2 = B\bar{x},\tag{3.10}$$

where $\bar{x} = (x-x_0)/2\theta$ and A and B are universal constants. The factor 2θ is used to normalize x because $2\theta = C_D d$, which is nearly equivalent to normalization by d since for circular cylinders $C_D \doteq 1$. Townsend (1956) and others used d in presenting their cylinder data.

According to Sreenivasan & Narasimha (1982), (3.7) and (3.8) may be written in the form

$$W = \frac{u_0}{U_\infty}\left(\frac{x}{\theta}\right)^{\frac{1}{2}}\tag{3.11}$$

and

$$\Delta = L_0(x\theta)^{-\frac{1}{2}}\tag{3.12}$$

where W and Δ are universal constants, provided the small-deficit, equilibrium wake is independent of initial conditions existing near the generator (see also Narasimha & Prabhu 1972). These parameters are related to the slopes in the relations (3.9) and (3.10) above. If we define W_0 and Δ_0 by (3.11) and (3.12), where x is replaced by $x-x_0$, then $A = 2/W_0^2$ and $B = 2\Delta_0^2$.

3.2. *Linear stability analysis*

The propagation of small-amplitude, wavy disturbances in a free shear layer was considered analytically by Bouthier (1972), Crighton & Gaster (1976), and Gaster *et al.* (1985). Since the analysis applied to the plane wake is identical to that presented in the latter reference, only the governing equations and essential features will be presented here.

The equation of motion considered is inviscid and has the following form

$$\frac{\partial \Omega}{\partial t} + U\frac{\partial \Omega}{\partial x} + V\frac{\partial \Omega}{\partial y} = 0,\tag{3.13}$$

where Ω is the vorticity and U and V represent the velocity components in the x- and y-directions, respectively. Upon neglecting the nonlinear terms, which are deemed to be small, and assuming that a given mean flow is parallel to the first order of approximation, the solution for the perturbation equation has a general form

$$\psi = \text{RP}\{\phi(y)\exp[\mathrm{i}(\alpha x - \beta t)]\},\tag{3.14}$$

where RP stands for the real part and the eigenfunction $\phi(y)$ is defined by the inviscid form of the Orr–Sommerfeld equation

$$\left[U(y) - \frac{\beta}{\alpha}\right](\phi'' - \alpha^2\phi) - U''(y)\phi = 0,\tag{3.15}$$

in which the primes denote differentiation with respect to y. The wave number α and the disturbance frequency β are eigenvalues determined by the solutions of (3.15),

which decay exponentially on both sides of the wake. Namely, the boundary conditions are

$$\phi'(\pm\infty)\pm\alpha\phi(\pm\infty) = 0. \tag{3.16}$$

Although the divergence of the mean flow may be partially controlled by the stresses resulting from the interaction with the disturbances present, within the realm of the linear approximation the slowly divergent mean flow is assumed to be prescribed by equations (3.1). Since the mean flow is assumed to be known, the conditions of self-preservation are not crucial to the analysis; the only requirement is that the derivatives of the mean stream function ψ with respect to x should be much smaller than the derivatives with respect to y (i.e. the boundary-layer approximation applies).

By analogy with the parallel flow problem, the perturbation solution has the form

$$\psi = \mathrm{RP}\left\{ A(x)\,\phi(x,y)\exp\left[\mathrm{i}\int_{x_0}^x \alpha(x)\,\mathrm{d}x - \beta t\right]\right\}, \tag{3.17}$$

where $\alpha(x)$ is a local wavenumber and the eigenfunction $\phi(x,y)$ changes only slowly with x. Since one expects the correction terms resulting from the slow divergence to be small, $\alpha(x)$ and $\phi(x,y)$ at a given streamwise location are still determined locally by (3.15), for which the mean velocity field $U(x,y)$ is known, and the correction term is defined by

$$A(x) = A_0 \exp\left[-\int_{x_0}^x \frac{N(x)}{M(x)}\,\mathrm{d}x\right],$$

where

$$N(x) = \int_{-\infty}^{\infty} \left\{ \beta\left[\phi\frac{\partial\alpha}{\partial x} + 2\alpha\frac{\partial\phi}{\partial x}\right] + U\left[\frac{\partial\phi''}{\partial x} - 3\alpha^2\frac{\partial\phi}{\partial x} - 3\alpha\phi\frac{\partial\alpha}{\partial x}\right] \right.$$
$$\left. + \phi'\frac{\partial U'}{\partial x} + U''\frac{\partial\phi}{\partial x} + V[\phi''' - \alpha^2\phi] \right\} \tilde{\phi}\,\mathrm{d}y, \tag{3.18}$$

and

$$M(x) = \int_{-\infty}^{\infty} \{2\alpha\beta\phi + U[\phi'' - 3\alpha^2\phi] - U''\phi\}\tilde{\phi}\,\mathrm{d}y,$$

where $\tilde{\phi}(x,y)$ is the adjoint function of $\phi(x,y)$ given by

$$\left[U(x,y) - \frac{\beta}{\alpha}\right][\tilde{\phi}'' - \alpha^2\tilde{\phi}] + 2U'\tilde{\phi}' = 0, \tag{3.19}$$

with the boundary conditions presented by

$$\tilde{\phi}'(\pm\infty)\pm\alpha\tilde{\phi}(\pm\infty) = 0. \tag{3.20}$$

When the mean velocity profile is symmetrical with respect to the line $y = 0$, the inviscid Orr–Sommerfeld equation admits both symmetrical (varicose) and antisymmetrical (sinuous) modes of disturbances. For parallel flow, one may take advantage of the symmetry and substitute a boundary condition on the centreline for the boundary conditions on one side of the wake,

$$\phi(0) = \tilde{\phi}(0) = 1, \quad \phi'(0) = \tilde{\phi}'(0) = 0, \tag{3.21}$$

for the sinuous mode of disturbance, or

$$\phi(0) = \tilde{\phi}(0) = 0, \quad \phi'(0) = \tilde{\phi}'(0) = 1, \tag{3.22}$$

representing the varicose mode. By virtue of the symmetry, one may usually confine attention to the semi-infinite interval $(0, +\infty)$ as in the parallel flow computations.

For a given real frequency β of the disturbance, the complex eigenvalues $\alpha(x)$ and eigenfunctions $\phi(x, y)$ and $\hat{\phi}(x, y)$ were evaluated at each of the streamwise locations of interest, provided the imaginary part $\alpha_i(x) < 0$ (i.e. the disturbances in the quasi-parallel flow approximation are amplified in the downstream direction), and these solutions were used in determining $A(x)$. The mean velocity field used in solving (3.15), (3.18) and (3.19) was obtained experimentally and was expressed by the exponential distribution

$$\frac{U}{U_\infty} = 1 - \frac{u_0}{U_\infty} \exp\left[-0.637\eta^2 - 0.056\eta^4\right], \tag{3.23}$$

where U_∞ is the free-stream velocity and $u_0(x)$ and $L_0(x)$ are the velocity and length scales discussed in §3.1. Despite the fact that the normalized shape of the velocity profile, $f(\eta)$, remained invariant for all wake generators considered, the eigensolutions had to be re-evaluated for each generator separately since $u_0(x)$ and $L_0(x)$ are dependent on the conditions at the generator, even for the small-deficit wakes.

Sato & Kuriki (1961) considered the temporal evolution of the small-amplitude, sinuous disturbance at a single location in the flow at which $(1 - u_0/U_\infty) = 0.692$. Mattingly & Criminale (1972) extended these calculations to both modes of instability evolving spatially and temporally at five prescribed locations in the immediate vicinity of the trailing edge of a flat-plate [i.e. for $0.44 > (1 - u_0/U_\infty) > 0$]. Since these computations are strongly dependent on u_0/U_∞, the solutions obtained are of little value in predicting the character of the amplified disturbances in the small-deficit wake for which $u_0/U_\infty \ll 1$. Furthermore, the assumption of parallel mean flow (i.e. the constancy of u_0/U_∞ and of L_0/θ) led to the general belief that the varicose mode has a negligible effect on the flow because its rate of amplification $(-\alpha_i)$ is smaller. It will be shown later that even a superposition of the two modes of instability leads to physically acceptable flow patterns associated generally with large coherent structures contained in the wake, in spite of the presence of the turbulent fluctuations, which was not considered in the calculations.

4. Experimental results

4.1. *General*

The mean flow field in the self-preserving region of a wake, the turbulence intensities, and Reynolds stresses were measured for a variety of two-dimensional wake generators. Data were obtained at distances ranging from 100 to 2000 momentum thicknesses downstream of the generator, where typical velocity deficits on the centreline of the wake varied from $0.15\,U_\infty$ to $0.03\,U_\infty$. The velocity at which the measurements were done varied from 7 to 20 m/s, corresponding to a range of Reynolds numbers based on the momentum thickness and the kinematic viscosity of air of 650 to 3200. In most instances, the shape and the size of the wake generators were tailored to provide a constant momentum thickness. The effects of Reynolds number and aspect ratio were examined separately in wakes generated by circular cylinders. Forced sinuous disturbances were generated in the wake of a symmetrical airfoil (having a maximum thickness to chord ratio of 30 %) and a flat plate (thickness to chord ratio of 2 %) by an oscillating, small flap mounted at the trailing edge. The results are summarized in table 2.

Wake generator	U_∞ (m/s)	θ (mm)	$\dfrac{x_0}{2\theta}$	W_0	Δ_0	$W_0 \times \Delta_0$
$\frac{3}{16}$ in. Cylinder	14.5	2.33	-74	1.75	0.289	0.506
30% Solidity screen	14.5	2.31	58	1.82	0.279	0.508
45% Solidity screen	14.5	2.33	27	1.78	0.285	0.507
70% Solidity screen	14.5	2.39	-21	1.67	0.302	0.504
Solid strip 100% solidity	14.5	2.31	-64	1.88	0.270	0.508
Symmetrical airfoil	14.5	2.34	-190	1.56	0.320	0.500
Flat plate	7.45	2.36	5	1.71	0.297	0.508
Flat plate flap freq. = 50 Hz AMP = 0.2 V	7.45	2.36	48	1.48	0.344	0.509
Flat plate flap freq = 50 Hz AMP = 0.3 V	7.45	2.46	61	1.32	0.382	0.504
Flat plate flap freq = 20 Hz AMP = 0.5 V	7.45	2.40	48	1.57	0.323	0.507
$\frac{3}{16}$ in. Cylinder (Chapman 1982)	20.7	2.54	-100	1.74	0.288	0.501
$\frac{1}{16}$ in. Cylinder	21.4	0.737	-170	1.77	0.285	0.504
$\frac{1}{16}$ in. Cylinder	14.5	0.737	-130	1.74	0.287	0.500

TABLE 2.

4.2. *The universality of the mean flow field in a small-deficit, plane wake*

The wake investigated most extensively is that generated by a circular cylinder, and therefore our investigation started with this wake generator. Some 400 momentum thicknesses downstream, the velocity scale u_0 was indeed proportional to $\bar{x}^{-\frac{1}{2}}$, and the width of the wake L_0 was proportional to $\bar{x}^{\frac{1}{2}}$, suggesting that similarity of the mean flow was indeed attained. The mean velocity profiles were plotted in the similarity coordinates and collapsed quite neatly onto a single curve described by the exponential function

$$f(\eta) = \exp\left[-0.637\eta^2 - 0.056\eta^4\right], \tag{4.1}$$

(figure 3). The exponential function traditionally used to describe the mean velocity profile {i.e. $f(\eta) = \exp\left[-0.693\eta^2\right]$} overestimates the mean velocity measured at the outer edges of the wake and, therefore, the fourth-order correction term was added. We expected the flow to be independent of Re when all lengthscales were normalized by the momentum thickness, and indeed the values of W_0 and Δ_0 were not affected by changes in Re ranging from $Re_d = 1360$ to $Re_d = 5900$. The aspect ratio of the cylinder was varied from 96 to 384 by changing the diameter of the cylinder and keeping the span constant (i.e. the distance between the sidewalls of the wind tunnel). The two-dimensionality of the mean flow field was checked at $\bar{x} = 430$ by comparing velocity and turbulence intensity profiles obtained at $z/L_0 = 0 \pm 7.5$ and was found to be satisfactory. The values of $W_0 = 1.75$ and $\Delta_0 = 0.287$ fitted quite well all wakes generated by a circular cylinder (the values were averaged over experimental points with $\bar{x} > 200$). This result would give credence to the universal equilibrium concept suggested by Sreenivasan & Narasimha (1982), except that the asymptotic values of
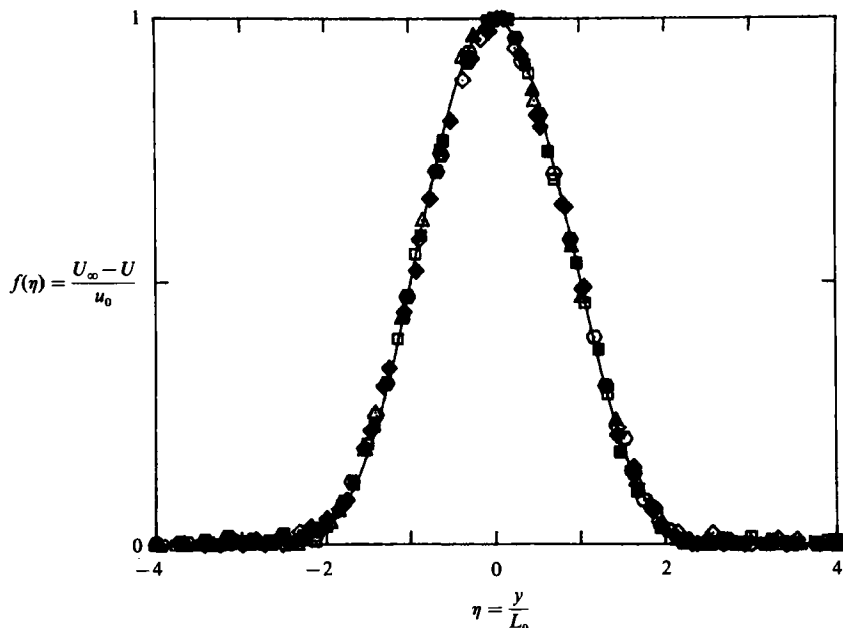
$$f(\eta) = \frac{U_\infty - U}{u_0}$$

$$\eta = \frac{y}{L_0}$$

FIGURE 3. The shape of the self-similar mean velocity profile. Data from 30 % solidity screen for $200 < \bar{x} < 700$.

the constants suggested by these authors were quite different, i.e. $W_0 = 1.63$ and $\varDelta_0 = 0.300$. The present data on the downstream development of the mean flow field behind a circular cylinder agree quite well with those obtained by Symes & Fink (1977) and Yamada et al. (1980), but only partially with Townsend's (1956) data. Our data on the mean wake growth, $L_0(x)$, agree with Townsend's but not the corresponding data on $u_0(x)$. It should be noted that there are very little data available on the mean wake growth and $u_0(x)$, even for circular cylinders, and this is undoubtedly attributable to the difficulty of obtaining such data.

The uniqueness of the mean velocity profile and the mean wake development for circular cylinders *in our facility* could lead to the conclusion that either the development of the plane, small-deficit wake is not susceptible to external disturbances or the velocity-dependent external disturbances in our wind tunnel (like the fan-blade passage-frequency, vibrations, etc.) are negligible within the range of variables considered. To answer this question, we could take our cylinders to other wind tunnels and repeat our experiments, but such testing could introduce new uncertainties over which we have no control. To avoid these difficulties, we addressed a related question. That is, in a given facility, are the x development of u_0 and L_0 dependent on the nature of the wake generator, holding all other controllable variables constant? We proceeded, therefore, to investigate wakes produced by a variety of two-dimensional generators. The first family of generators considered were screens with solidity ratios ranging from 30 to 100 % (a thin metal strip placed normal to the free stream). The porous screens have numerous advantages: (i) there is no flow reversal in the vicinity of the generator with all its ensuing experimental complications; (ii) the porous screens do not generate vortices in the same way as the circular cylinders do and, therefore, their drag should not be as sensitive to Reynolds number; (iii) the roll-up of vortices in the mixing layers generated in the neighbourhood of the screens is, in
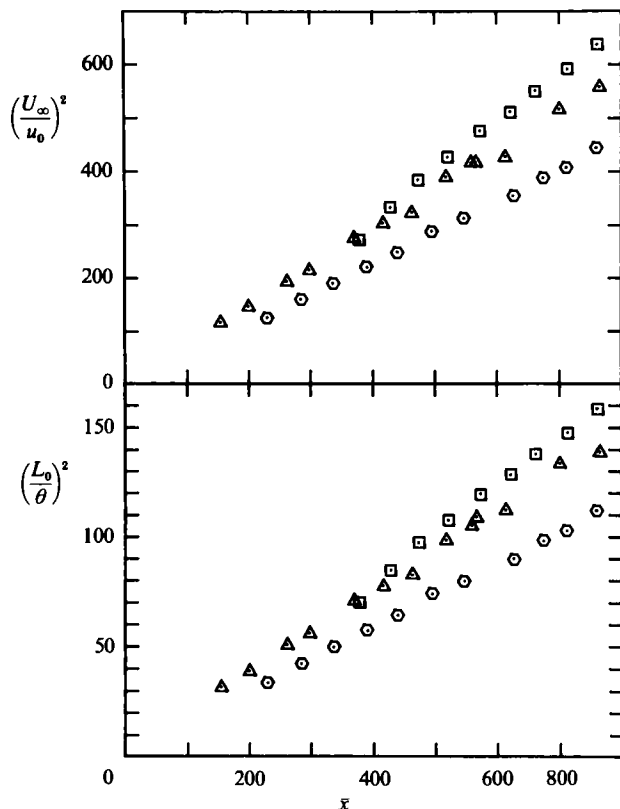
FIGURE 4. The variation of u_0 and L_0 with $\bar{x}$ for three wake generators; $\square$, airfoil; $\triangle$, 70% solidity screen; $\bigcirc$, solid strip.

principle, predictable and dependent on the solidity (Gaster *et al.* 1985); and (iv) the drag of screens having a different solidity can easily be equated by altering the size of the screens. It was decided to maintain the momentum thickness of all four screens constant in order to avoid any questions about the unknown effects of Reynolds number or aspect ratio in the development of the plane, small-deficit wake. The results show that the shape of the normalized mean velocity profile is identical to that obtained for the circular cylinder in all cases considered, yet the values of W_0 range between 1.67 for the 70% solidity screen to 1.88 for the limiting case representing the solidity of 100%.

The value of W_0 decreases with increasing solidity of the screens, provided the porosity suffices to prevent flow reversal in the lee of the screen; however, the value of W_0 for the solid strip (which is regarded as a screen having 100% solidity) is higher than the value of W_0 for the most porous screen investigated (solidity of 30%). This result is attributed to the observed alternate shedding of vortices from the two separation points on the strip. The determination of the threshold solidity beyond which an alternate shedding of vortices starts to occur is not within the scope of the present investigation.

In the absence of periodic forcing, the lowest W_0 measured in this experiment was attained in the wake of a non-lifting, thick, symmetrical airfoil section. The mean velocity field in the wake of the flat plate was nearly identical to the velocity field produced by the wake of a circular cylinder except for the location of the virtual origin
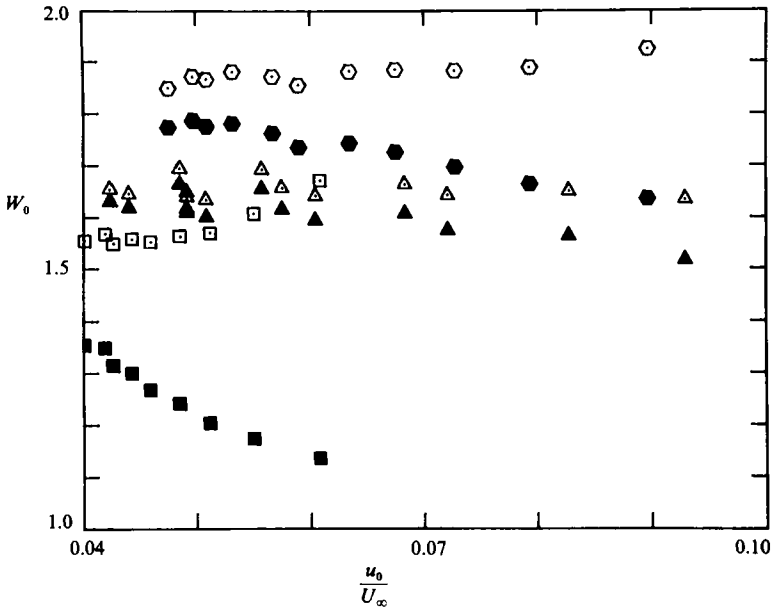
FIGURE 5. The variation of w_0 with u_0/U for three wake generators; $\square$—$\blacksquare$, airfoil; $\triangle$—$\blacktriangle$, 70 % solidity screen; $\odot$—$\bullet$, solid strip.

x_0. The introduction of periodic surging reduced the effective W_0 from 1.71 to 1.56 without affecting the overall drag experienced by the body (i.e. the product $W_0\, \varDelta_0$). The location of the virtual origin moved downstream with increasing amplitude of the forced oscillations (table 2).

The product $W_0\, \varDelta_0$ represents the conservation of momentum within the context of the linearization and, therefore, its constancy for all wake generators ($W_0\, \varDelta_0 = 0.506 \pm 0.002$) reaffirms the suggestion that the normalized shape of the mean velocity profile (figure 3) is universal for all the wake generators considered. Some examples of the variation of $(U_\infty/u_0)^2$ and $(L_0/\theta)^2$ with $\bar{x}$ are shown in figures 4(a) and (b), respectively, establishing that the coefficients of proportionality A and B [(3.9) and (3.10)] or W_0 and $\varDelta_0$ depend on the wake generator.

The mean velocity in the wake obeys the similarity scaling for $\bar{x} > 400$. The different slopes of the lines drawn in figure 4(a) result in a diversity of estimates for W_0 (figure 5), varying between 1.5 and 1.9 depending on the wake generator. The differences are large and are not attributable to experimental inaccuracy.

Only one value of x_0 was chosen for each wake generator, and it had to satisfy the dependence of both u_0 and L_0 on initial conditions. The choice of x_0 does not affect the dependence of W_0 or $\varDelta_0$ on the initial conditions, although the absolute values of W_0 and $\varDelta_0$ may vary slightly if improper values of x_0 were used. Figure 5 demonstrates this point. The open symbols refer to physical distances measured from the trailing edge of the generator (i.e. $x_0 = 0$), and therefore the values of W_0 based on these data define a sloping curve rather than a horizontal line. This effect is particularly severe whenever x_0 is large, as it is in the wake of the symmetric airfoil. It is apparent, therefore, that for the range of distances considered, the mean flow in the plane, small-deficit, turbulent wake is dependent on the initial conditions set up by the generator.

The preservation of momentum deficit in the wake produced by all the generators
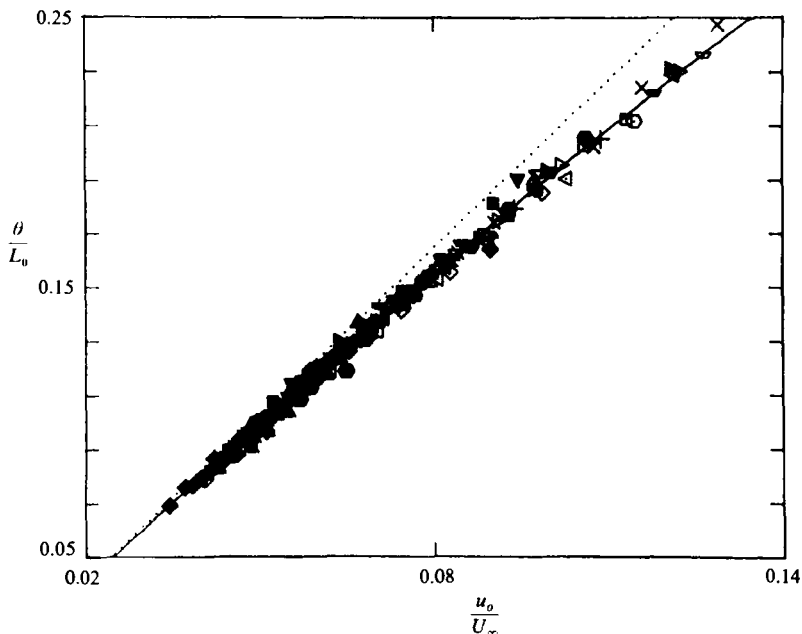
FIGURE 6. The dependence of θ/L_0 on u_0/U_∞. Symbols represent data from all wake generators studied.

considered above is illustrated by plotting θ/L_0 versus u_0/U_∞ (figure 6). For similar velocity profiles,

$$\frac{\theta}{L_0} = \frac{u_0}{U_\infty}\left(\mathscr{I}_1 - \frac{u_0}{U_\infty}\mathscr{I}_2\right),$$ (4.2)

with $\mathscr{I}_n$ as defined in (3.6).

Equation 4.2 describes a parabola (a solid curve in figure 6), while the linear approximation $(\theta/L_0)\,(U_\infty/u_0) = \mathscr{I}_1$ is drawn as a dotted line. The values of $\mathscr{I}_1$ and $\mathscr{I}_2$ are 2.06 and 1.505, respectively, and are in excellent agreement with the data of Sreenivasan & Narasimha (1982). Measured values of θ/L_0 follow quite clearly the parabolic curve for all $u_0/U_\infty < 0.14$. One can obtain an expression for θ/L_0 by eliminating $\bar{x}$ from (3.9) and (3.10), which yields

$$\frac{\theta}{L_0} = \frac{1}{W_0\,\varDelta_0}\frac{u_0}{U_\infty}.$$ (4.3)

The quantity $(1/W_0\,\varDelta_0)$ was found to be 1.97 as opposed to $\mathscr{I}_1 = 2.06$, and therefore (4.3) represents a better approximation to the data than does the linear approximation to (4.2).

4.3. *The lack of universality of the turbulent field*

For a self-preserving wake (Townsend 1956), the transverse distributions of the intensities and Reynolds stresses are given by (3.1), where the g functions are supposedly universal functions analogous to $f(n)$. In particular, the longitudinal component of the turbulent intensity and the shear stress are given by

$$\overline{u^2} = u_0^2\,g_{11}(\eta),$$ (4.4)

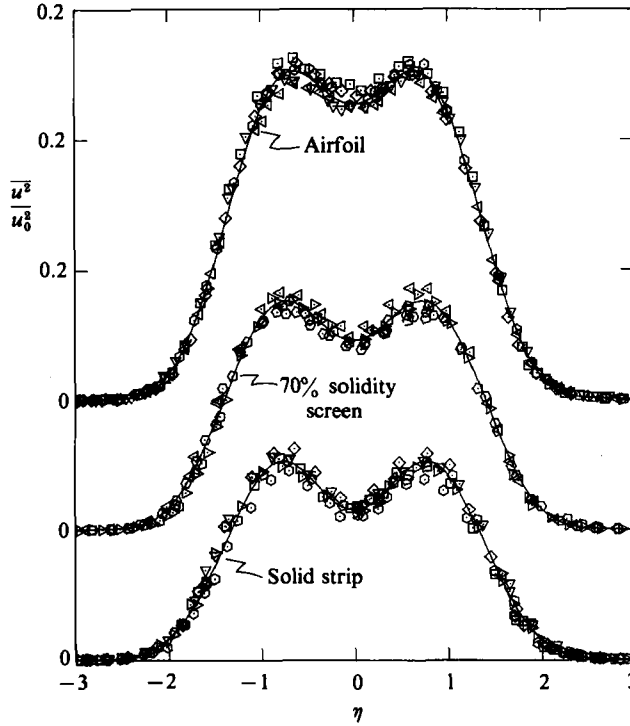$$\overline{uv} = u_0^2\,g_{12}(\eta).$$ (4.5)

FIGURE 7. The measured distributions of $g_{11}(\eta)$ for the solid strip, the 70 % solidity screen, and the symmetric airfoil. The different symbols represent different downstream locations. The solid lines represent the best fit to each data set.

The measured distributions of $g_{11}(\eta)$ for the solid strip, 70 % solidity screen, and the symmetric airfoil are shown in figure 7. The data indicate that although each wake is approximately self-similar, the function $g_{11}(\eta)$ depends on the nature of the wake generator. To elucidate the differences in the measured $\overline{u}^2$ distributions, we plotted a normalized function defined by

$$\overline{u}^2 = \overline{u}^2_{\max} G_{11}(\eta), \tag{4.6}$$

which is shown in figure 8 for the three data sets. A good measure in assessing the lack of universality is the ratio $\overline{u}^2_{\mathrm{CL}}/\overline{u}^2_{\max}$ (where the subscript CL refers to the centre plane of the wake), which varies from 0.76 for the solid strip to 0.9 for the airfoil. This ratio is correlated with the rate of spread of the wake or the decay of the mean velocity on the centreline.

The degree to which each of the wakes approaches a self-preserving state can be determined from figure 9, which shows the downstream variation of the square root of $\overline{u}^2_{\max}/u^2_0$. For a self-preserving state, this statistic should be a constant, independent of x. Notice that the wake behind the solid strip reaches a self-preserving state more rapidly than the wakes behind the screen or airfoil. (Recall that the airfoil wake has a large negative value of x_0.) The self-preserving nature of $g_{12}(\eta)$, the normalized shear stress, for the airfoil can be determined from figure 10, where stress distributions at 8 downstream locations in the range $485 < \overline{x} < 800$ are presented. Similar results were obtained for the solid strip and 70 % solidity screen. These data were obtained at a free-stream velocity of 7.5 m/s, rather than 14.5 m/s, because we had better control
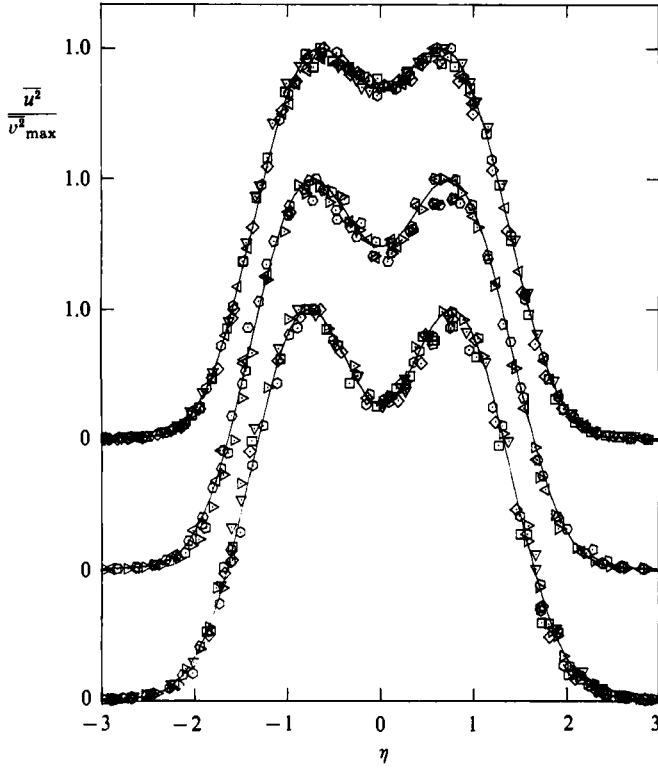
FIGURE 8. The normalized turbulent intensity distributions for the three generators. The value of $\bar{u}^2_{\mathrm{CL}}/\bar{u}^2_{\mathrm{max}}$ for each generator is indicated. The solid lines represent the best fit to each data set.
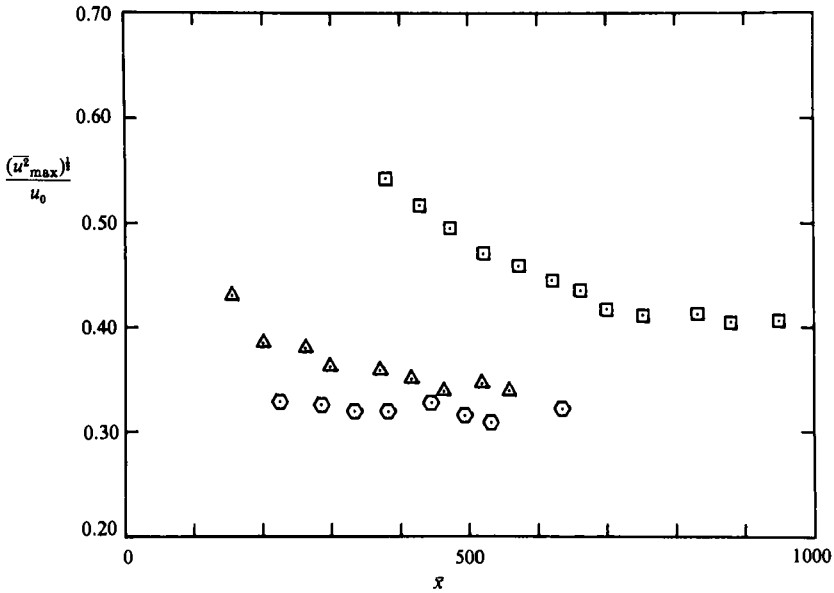
FIGURE 9. The downstream variation of $(g_{11,\mathrm{max}})^{\frac{1}{2}}$ for the three generators; $\square$, airfoil; $\triangle$, 70 % solidity screen; $\odot$, solid strip.
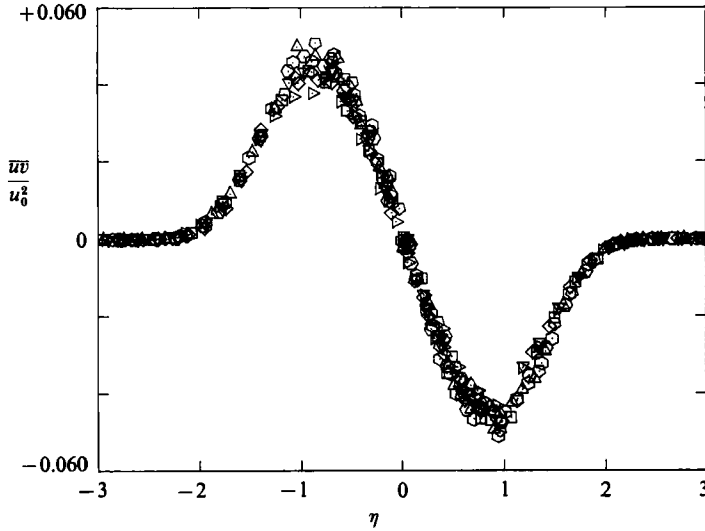
FIGURE 10. The measured distributions of $g_{12}(\eta)$ for the airfoil at eight downstream locations.

of the temperature of the airflow at the lower velocity. The temperature was maintained to within ± 0.1 °C of the calibration temperature for the X-wire runs. The corresponding Reynolds numbers, Re_θ, for the airfoil are 1260 and 1996, respectively, and certainly no significant change in the flow structure occurs between these Reynolds numbers. The function $g_{12}(\eta)$ attains a self-preserving shape more rapidly than does $g_{11}(\eta)$ for all three wake flows.

A link between the variation in the spreading rate of the mean flow and $g_{12}(\eta)$ in the self-preserving region can be obtained from the mean momentum equation, which in linearized form is given by

$$f + \eta f' = \frac{2W_0}{\varDelta_0} g_{12}'. \tag{4.7}$$

This equation can be integrated to yield

$$g_{12}(\eta) = \frac{\varDelta_0}{2W_0} \eta f. \tag{4.8}$$

Note that $\varDelta_0/2W_0$ varies by 43 % between the solid strip and the symmetric airfoil and, therefore, $g_{12}(\eta)$ must also differ by this amount, as $f(\eta)$ is a universal function. Reynolds stress distributions were measured at one downstream x-location for the two wake generators. The downstream location chosen corresponds to $\bar{x}$ values of 614 and 733 for the solid strip and airfoil, respectively, well within the self-preserving region for each wake. The Reynolds number for the measurements is the nominal 2000, the value used to obtain the $\varDelta_0$ and W_0 data. Figure 11 shows the measured values of $\overline{uv}/u_0^2$ for the two generators. The solid lines represent the theoretical prediction for each wake based on the linearized momentum equation and $f(\eta)$, i.e. (4.8). Note that the distribution for the airfoil definitely has larger values than that for the solid strip. Similar data were also obtained for the 70 % screen and the results fell between those for the solid strip and airfoil, which is consistent with (4.8). The agreement between the data and the linearized theory provides convincing evidence for the lack of universality of the turbulent structure of two-dimensional far wakes.
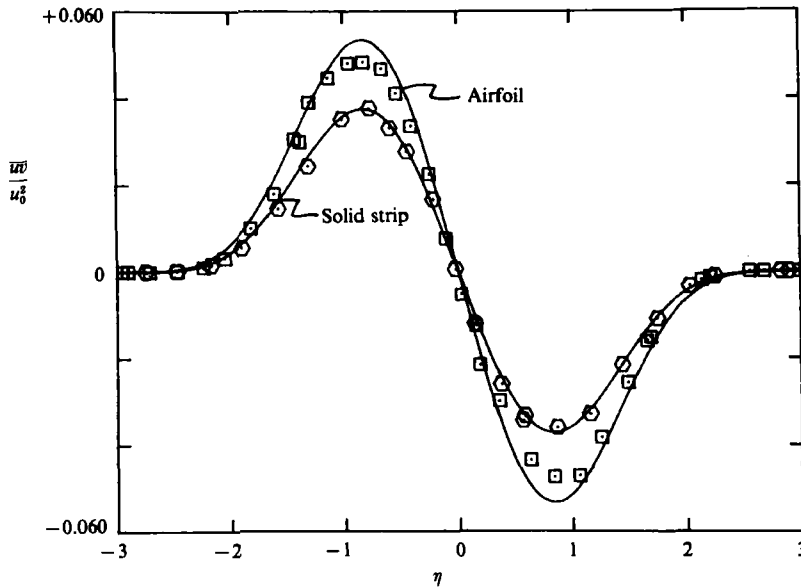
FIGURE 11. The distributions of $\overline{uv}/u_0^2$ for the solid strip and the airfoil. The solid lines represent the linearized theory prediction, equation (4.8). $\square$, airfoil, $\bar{x} = 733$; $\odot$, solid strip, $\bar{x} = 614$.

Indeed, the lack of universality of $\overline{u^2}_{\mathrm{CL}}$ presented by various investigators for the circular cylinder triggered the present investigation (figure 2). The peculiar shape of $G_{11}(\eta)$, which has a local minimum at $\eta = 0$, is associated with a distribution of large vortices about the centreline of the wake (see Sato & Kuriki 1961; Wygnanski, Oster & Fiedler 1979). It was therefore anticipated that large coherent structures which retain their characteristic shape and associated velocity perturbation are responsible for the apparent dependence of the wake on the conditions at its origins.

4.4. Spectra and normal modes of instability

Spectra of the streamwise component of the velocity fluctuations were measured at several $\bar{x}$ locations in the wake behind the flat plate. The measurements presented in figure 12 were taken on the centreline at $102 < \bar{x} < 587$, while the spectra in figure 13 were measured along a curve representing the outer boundary of the wake, i.e. at $\eta = 3$. Only the most significant decade of the spectra has been plotted. The abscissa on these figures is frequency plotted on a logarithmic scale, while the ordinate is $fF(f)$ in order to represent the relative contribution to the streamwise component

of intensity at a given frequency f [i.e. $\overline{u^2} \propto \displaystyle\int F(f)\,\mathrm{d}f = \int fF(f)\,\mathrm{d}\,(\log f)$].

   The spectra measured on the centreline of the wake (figure 12) have a shape which is typically observed in any unbounded, turbulent, shear flow (Champagne 1978). The spectral distribution is broad, and the frequency range associated with the most energetic eddies gradually moves toward lower frequencies as the flow develops in the downstream direction. The insert in figure 12 shows a log–log plot of the normalized (to unity) spectra $F(f)$. The frequency has been rendered non-dimensional using the local length scale, L_0, and U_∞. The similarity of the spectral distribution indicates that the length scales associated with the energy-containing eddies ($\lambda = U_\infty/f$) are proportional to the width of the wake, L_0, which is therefore an
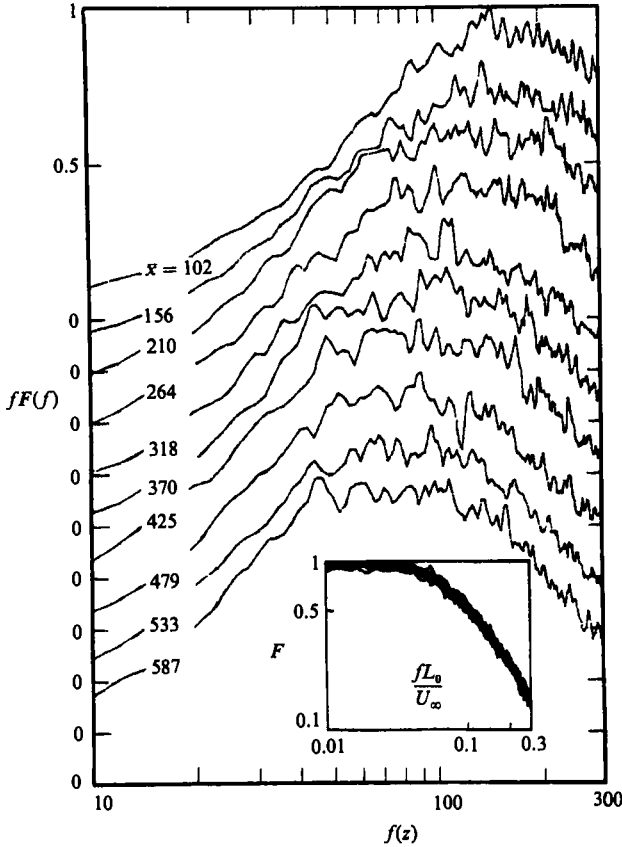
FIGURE 12. Spectra of u fluctuations on centreline of flat-plate wake at various downstream positions. Insert shows similarity of spectra when scaled by L_0 and U_∞.

appropriate characteristic lengthscale for comparing the mean velocity profiles generated by various obstacles.

The spectral measurements at $\eta = 3$, shown in figure 13, represent fluctuations induced by the passage of the large turbulent structures in the wake since the coordinate $\eta = 3$ is located outside the turbulent interface. The insert in this figure shows that, as with the centreline spectra, these spectra also scale with the local width L_0. Note the shift of the spectral peaks toward lower frequency with increasing $\bar{x}$.

Equation (3.15) was solved for the prescribed local mean velocity field and numerous real frequencies to obtain the variation of the spatial rate of amplification $(-\alpha_i)$ with increasing distance from the flat plate. The results of these computations indicate that the maximum local amplification rate shifts toward lower frequencies with increasing $\bar{x}$. Figure 14 shows the spatial amplification rates for different frequencies. The value of $\bar{x}$ for which a constant frequency line intercepts the $\bar{x}$-axis (i.e. $\alpha_i = 0$) corresponds to the streamwise location at which a wave at that frequency has undergone a maximum amplification according to locally parallel, linear, inviscid stability theory. A plot of these intercepts versus frequency, shown also in figure 14, represents the dependence of the expected predominant frequency in the wake on the distance from the trailing edge of the flat plate. The measured predominant frequency range, defined as those frequencies at $\eta = 3$ whose amplitude is within 90 %
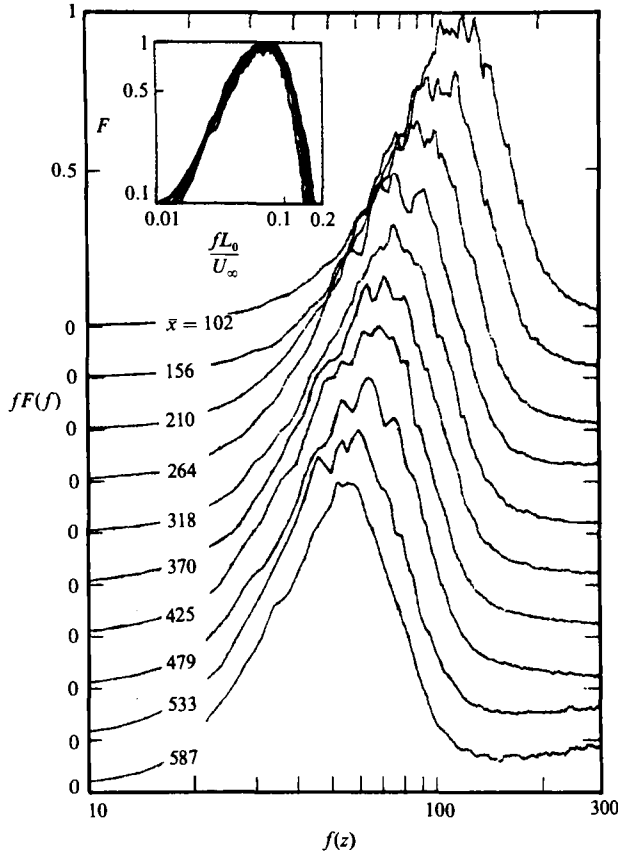
FIGURE 13. Spectra of induced u fluctuations at $\eta = 3$ in the flat-plate wake at various downstream locations. Insert shows similarity of spectra when scaled by L_0 and U_∞.

of the peak energy value, are plotted in figure 14 and compared with the computed results. The dashed lines show the measured predominant frequency range determined for $\eta = 0$. The good agreement between the measured predominant frequencies associated with the passage of the large coherent structures and the most-amplified frequencies calculated using linear stability theory suggest that the large structures observed in this flow may be related to the two-dimensional instability modes.

4.5. *The amplification of imposed sinuous oscillations*

Two-dimensional sinusoidal oscillations in the direction normal to the mean flow were generated by the motion of a small flap hinged to the trailing edge of the flat plate. The frequency of the imposed oscillation was matched to the expected most-amplified fluctuations measured at $\eta = 3$ in the region of interest. A typical power spectrum measured with and without excitation is presented in figure 15. Small-amplitude oscillations do not affect the turbulent intensity in the wake nor do they affect the shape of the spectral distribution. The two spectra presented in figure 15 are almost identical, with the exception of the peak corresponding to the frequency of the excitation.

In order to be sure that the instability mechanism in the wake is actually responsible for the amplification of the imposed oscillations, measurements of spectra
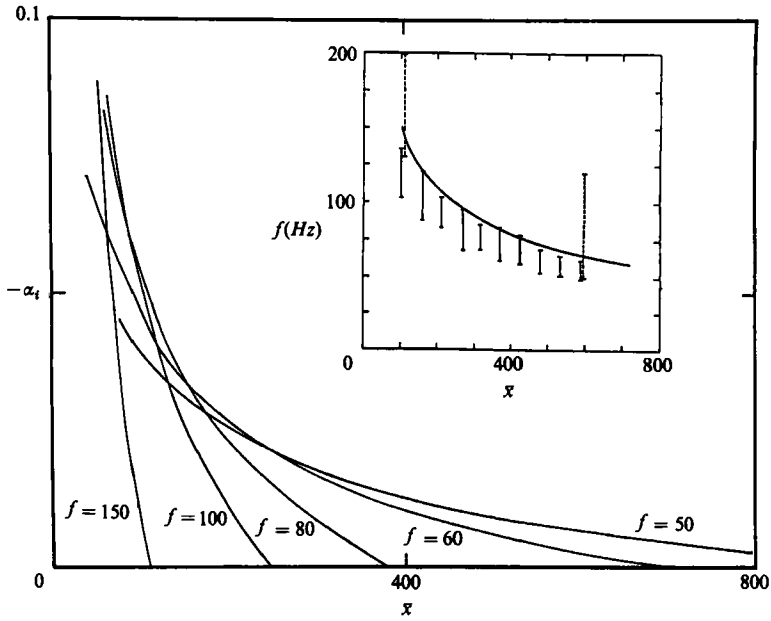
FIGURE 14. Spatial amplification rates computed for several disturbance frequencies in a wake. Insert shows expected predominant frequency (computed) compared to measured predominant frequency range as a function of $\bar{x}$.
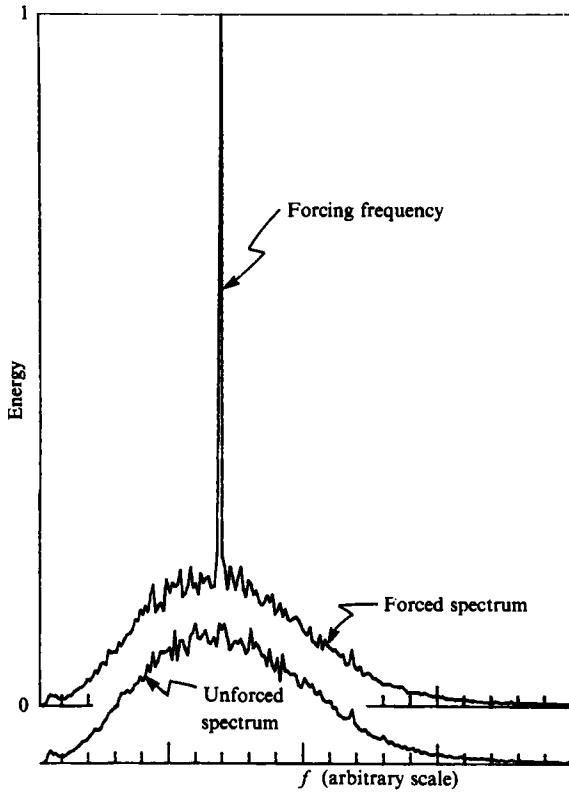

FIGURE 15. The effect of forcing on the measured u spectrum at $\bar{x} = 400$.

$$\frac{f}{f_{ma}} = \tfrac{5}{4} \qquad \frac{f}{f_{ma}} = \tfrac{9}{8} \qquad \frac{f}{f_{ma}} = 1 \qquad \frac{f}{f_{ma}} = \tfrac{7}{8} \qquad \frac{f}{f_{ma}} = \tfrac{3}{4}$$
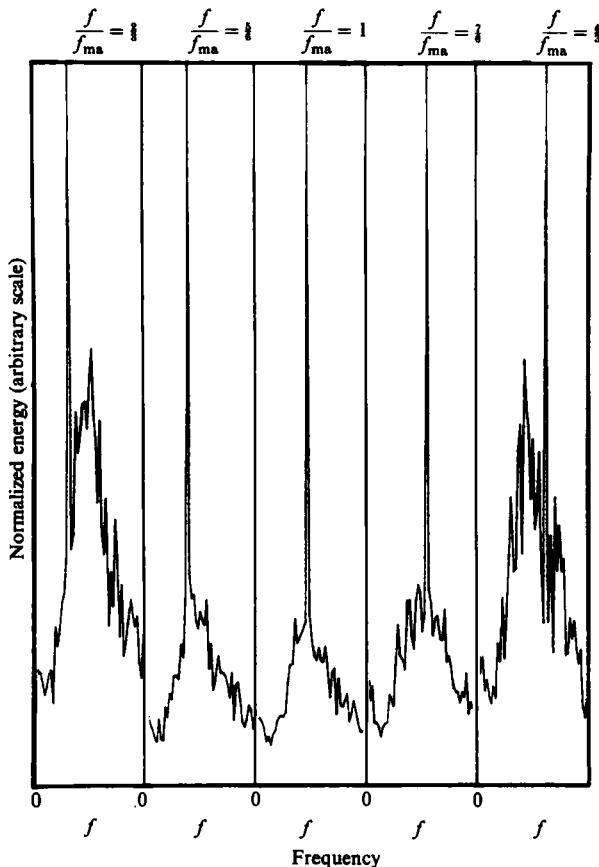

FIGURE 16. The effect of forcing frequency on the velocity spectrum at a fixed location in the wake. $\bar{x} = 400$.

were repeatedly taken at one location in the flow for a variety of forcing frequencies while all other controlled variables were unchanged. Since the background turbulence level is not significantly affected by the introduction of forcing (figure 15), the ratio of the amplitudes between the imposed wave and the background exhibits the sensitivity of the wake to the imposed sinuous perturbations. The normalized spectrum in the centre of figure 16 shows the ratio of amplitudes for the most-amplified frequency at the location considered. When the frequency of forcing was either higher or lower than the most-amplified frequency for the given location and flow conditions, the ratio between the peak amplitude and the background diminished. In view of the symmetry of the response around the most-amplified frequency (figure 16), which was repeated at other flow conditions (and therefore other frequencies), the possibility of resonance of the mechanical flap system was discarded.

The amplitude and phase of an artificially excited sinuous wave at a frequency corresponding to $f\theta/U = 6.4 \times 10^{-3}$ ($f = 20$ Hz) were calculated for the wake of the flat plate. The mean flow required for the solution of (3.15), (3.18) and (3.19) was provided by (4.1) and table 2 (i.e. $W_0 = 1.57$, $\varDelta_0 = 0.323$, $\bar{x}_0 = 48$). These equations were solved at intervals of $\bar{x} = 10$ for a rectangular window starting at $\bar{x} = 250$ and ending at $\bar{x} = 750$ and at intervals of 0.1 between $-40 \leqslant y/2\theta \leqslant 40$. For a given frequency ($\beta = 2\pi f(L_0)_{\bar{x}=750}/U_\infty$), the eigenvalues $\alpha(x)$ and eigenfunctions $\phi(x,y)$ and
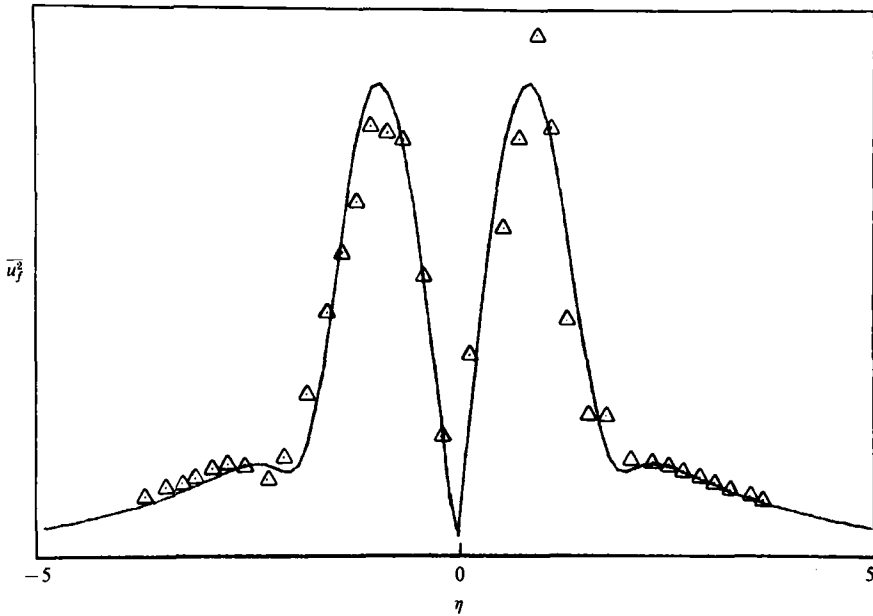
FIGURE 17. Amplitude distribution of u fluctuations phase locked to the external sinuous forcing signal. $\bar{x} = 400$.
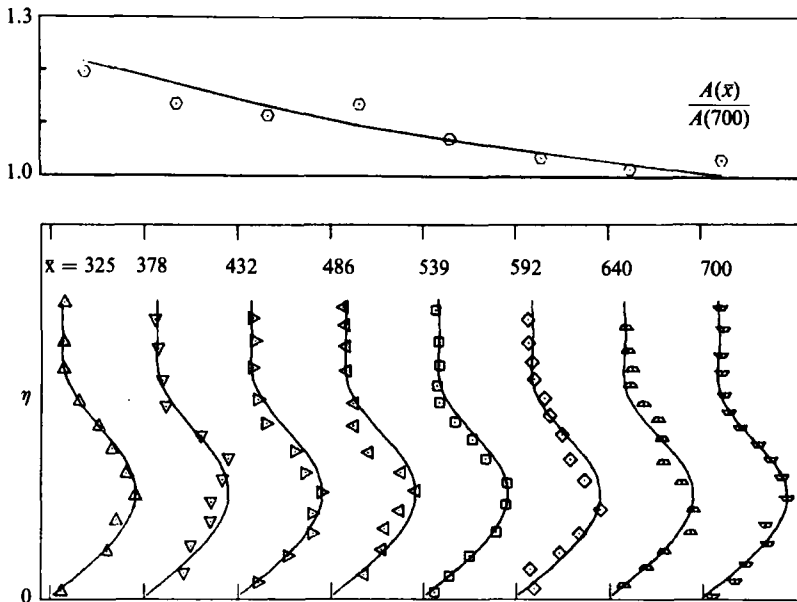

FIGURE 18. A comparison between the measured and predicted u perturbation amplitude distributions at several $\bar{x}$ locations in a sinuously forced wake. A is not $A(x)$ of theory.

$\tilde{\phi}(x, y)$ were evaluated at each of the 51 streamwise locations. These functions, their derivatives with respect to both x- and y-coordinates, and the mean flow information were used to determine the correction term for slowly divergent flow $A(x)$ (equation (3.18)). Only the streamwise component of the velocity perturbation was measured and compared with the calculations.
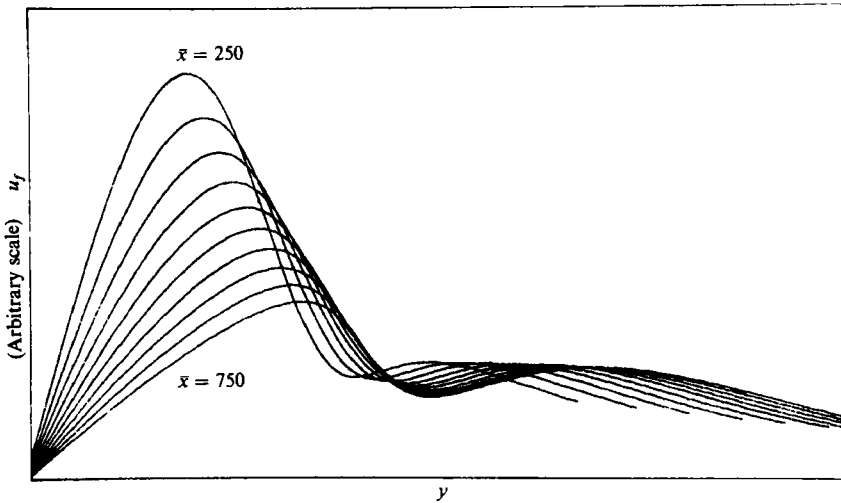
FIGURE 19. The variation of the computed eigenfunction with $\bar{x}$. $U_\infty = 7.4$ m/s; $\theta = 2.36$ mm; $f = 40$ Hz; $St = f\theta/U_\infty = 0.0128$.

A typical distribution of normalized amplitudes of the sinuous mode across the entire wake is shown in figure 17. The solid line represents computed values, while the triangles represent experimental results at $\bar{x} \sim 500$. The data were acquired by recording the velocity, together with the sinusoidal signal activating the flap. The velocity signal was phase-averaged over 300 cycles of the flap motion, and the Fourier transform of these average records provided the phase and amplitude estimates of the spectral elements of the velocity field, which were quite free from the random, turbulent fluctuations present in the original signals. There is little doubt that the artificially excited wavetrain can be described by an inviscid linear model, in spite of the fact that the flow is fully turbulent. One may note that the measured amplitude distribution in figure 17 is not exactly symmetrical about the centreline; the lack of symmetry is partly attributed to interference between the probe holder and traversing mechanism, to the large structures in the wake, and to the presence of the varicose mode.

A detailed comparison between the predicted amplitude distribution of the forced wave and measured amplitude profiles at eight streamwise locations is shown in figure 18. In the bottom part of this figure, the velocities were normalized by their respective maxima, which are replotted at the top. The computed maximum amplitude at $\bar{x} = 700$ was assigned the value of unity, which is the only floating constant in this comparison. The predicted and measured lateral distributions of amplitudes are in good agreement with one another, as is the decay of the maxima with increasing distance from the generator. It was surprising, at first, to note that the maximum amplitude of the forced wave actually diminished with $\bar{x}$, in spite of the fact that the quasi-parallel solutions based on (3.14) would predict amplification ($\alpha_i < 0$). The reasons for the apparent anomaly stems from the fact that α_i is a small negative number in the range of distances considered, and it is outweighed by the shape of the eigenfunction whose maximum amplitude diminishes with increasing $\bar{x}$ (figure 19). A similar observation for an axisymmetric jet was made by Strange (1982). The value of the integral of the perturbation amplitude across the wake increases somewhat with increasing $\bar{x}$ because the width of the wake increases. In fact, the product of the
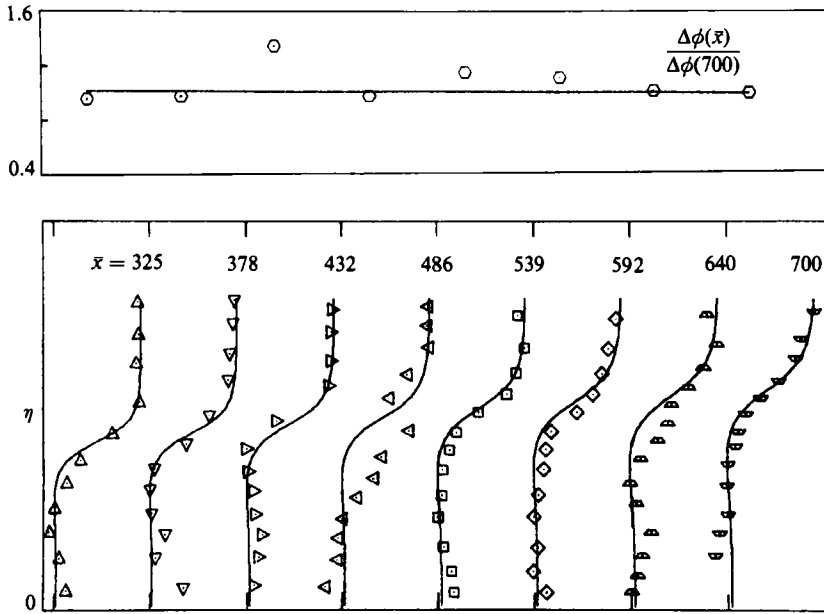
FIGURE 20. A comparison between measured and predicted phase distributions in a wake.

maximum amplitude and the local width is nearly constant between $\bar{x} = 325$ and $\bar{x} = 700$. This result could not have been predicted by the parallel flow approximation because it is sensitive to dL_0/dx and to u_0/U_∞. The corresponding measured and computed phase profiles are shown in figure 20.

The amplification of a forced wavetrain in a turbulent, plane wake agrees in principle with similar observations made by Sato & Kuriki (1961) and Mattingly & Criminale (1972) for the growth of small disturbances in a laminar wake. In fact, only qualitative agreement was obtained by Mattingly & Criminale between experimental measurements and the predictions of the linearized spatial stability approach, while quantitative agreement is seen in the present case. Although improvements were made in both theory (inclusion of slow divergence) and experiment (forcing a sinuous mode), the type of agreement shown would not have been possible if the interaction between the imposed two-dimensional disturbances and the small-scale, three-dimensional turbulence in this flow was significant. Mattingly & Criminale attributed the discrepancies they observed to the inviscid assumption and to the neglected longitudinal gradients in the mean wake profiles; it seems to us that the inviscid assumptions can be retained as long as one considers waves which would have been growing spatially in parallel flow.

4.6. *The amplification of natural disturbances in a plane, turbulent wake*

Encouraged by a successful prediction of the propagation of imposed two-dimensional perturbations in this flow and intrigued by the shape of the broadband distribution of $\bar{u}^2$ in the wake, we proceeded to analyse the propagation of two-dimensional disturbances occurring naturally in a wake. In this case, the entire turbulent signal was Fourier analysed, instead of the phase-locked average considered in §4.5, and a particular spectral component corresponding to $f\theta/U_\infty = 1.3 \times 10^{-2}$ was examined in detail. The frequency chosen ($f = 40$ Hz at $U = 7.4$ m/s) corresponded approxi-
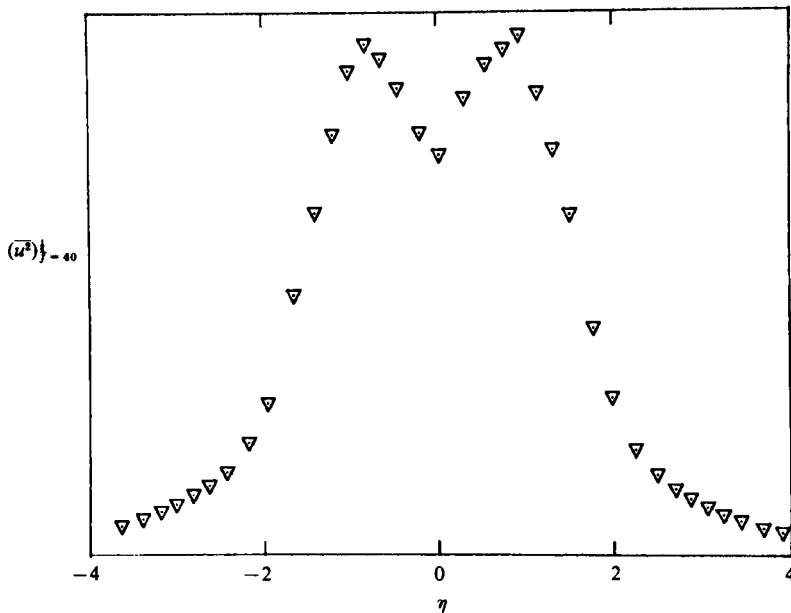
FIGURE 21. The amplitude distribution of the u component $f = 40$ Hz and $\bar{x} = 587$ in the unforced wake.

mately to the anticipated most-amplified sinuous mode in the range of $\bar{x}$ considered. A typical profile of $(\overline{u_f^2})^{\frac{1}{2}}$ in the wake of a flat plate corresponding to $\bar{x} = 587$ is shown in figure 21. The resulting lateral distribution of amplitudes of $(\overline{u_f^2})^{\frac{1}{2}}$ is quite similar to the broadband distribution of u^2 shown in figure 7, although the ratio $[(\overline{u_f^2})_{\text{CL}}/(\overline{u_f^2})_{\text{max}}]$ is generally lower than the corresponding broadband distribution. Because the data are no longer phase locked, the actual amplitudes plotted are much larger than for the imposed wavetrain. Since the calculated amplitudes do not vanish on the centreline of the wake as predicted by the sinuous mode of inviscid amplification, another mechanism has to be considered. A hint was provided by the fact that the amplification rates $(-\alpha_i)$ predicted on the basis of the parallel flow approximation were overwhelmed by the presence of longitudinal gradients in the mean flow (figure 17). It seems plausible that the same longitudinal mean flow gradients may have enhanced the relative importance of the varicose mode, which would contribute to the amplitude of the fluctuations on the centreline; otherwise, nonlinear effects and secondary instabilities may have to be considered.

The calculation procedure outlined in §4.4 was repeated for $f\theta/U_\infty = 1.3 \sim 10^{-2}$ and the appropriate mean flow parameters (table 2). The calculations were done twice; once for the sinuous motion, then a second time for the varicose mode. By assuming that, to the first order of approximation, one may simply superimpose the amplitudes of the individual modes of instability, neglecting any correlation between them, the resulting amplitudes were calculated. For the purpose of comparison between computations and experiment, it was assumed that the initial amplitudes resulting from both modes are equally important; namely, that the maximum amplitude of the varicose mode is equal to the maximum amplitude of the sinuous mode at some initial $\bar{x}$-distance from the generator. The results of these calculations are plotted in figure 22 for $370 \leqslant \bar{x} \leqslant 640$; the symbols in the figure represent data calculated from experimental results and filtered at $f\theta/U_\infty = 1.3 \sim 10^{-2}$. There is a qualitative
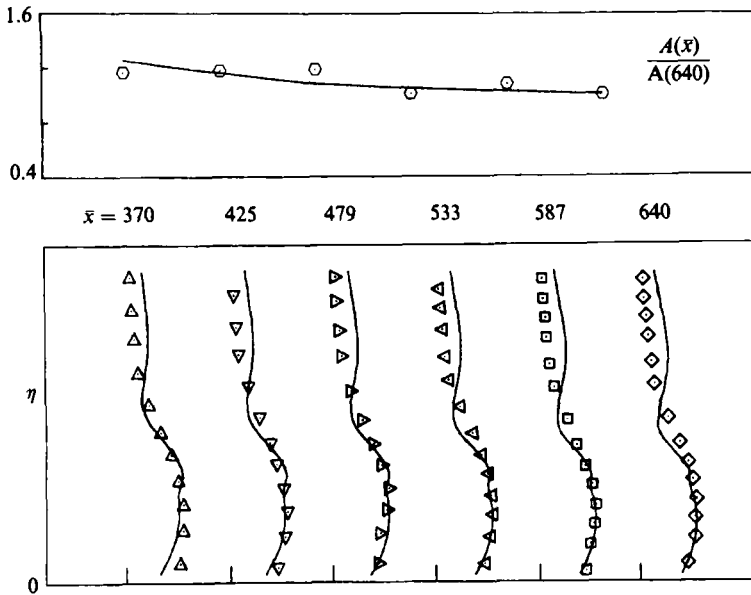
FIGURE 22. A comparison between measured and predicted u amplitude distributions at several $\bar{x}$ locations in an unforced wake. A is not $A(x)$ of theory.

FIGURE 23. Large coherent structures photographed in the wake of the flat plate with no forcing. $\bar{x} \simeq 500$ and $Re_\theta = 600$.

agreement between the predicted and measured lateral distributions of the $\bar{u}_f^2$ amplitudes, indicating that both modes of instability are probably present and can give rise to the peculiar profile of the u fluctuations in the wake. The agreement between theory and experiment in this case is not as good as for the forced sinuous wave, suggesting that either the two-dimensional approximation is invalid or the simple linear superposition neglecting the phase relation between both modes is inadequate. Another possible error stems from the nonlinear terms neglected in the present context.

In order to explore further the importance of the interaction between the two modes of instability, we resorted to flow visualization using a smoke wire. The wire was

positioned at $\bar{x} = 350$, while the camera was located at $\bar{x} = 500$. The smoke patterns were photographed at $U_\infty = 3.4$ m/s (corresponding to $Re_\theta = 600$), rather than at $U_\infty = 7.45$ m/s to enhance the quality of the results. The smoke wire did not work well at the higher velocity. Although θ is approximately 20% higher for the lower Reynolds number, this case is representative for the larger Reynolds number case ($Re_\theta = 1035$) as the large-scale turbulence should be relatively insensitive to the Reynolds number change used here. Large coherent structures are clearly visible in the wake of the flat plate (figure 23), even in the absence of any imposed oscillations. These structures are similar in appearance to the Karman vortex street because they seem to be comprised of vortices of alternating sign of vorticity, which are placed in a staggered manner on both sides of the wake centreline. Therefore, neither the varicose mode, which requires that the vortices appear in pairs distributed symmetrically about the centreline, nor the sinuous mode, which requires vortices whose centre coincides with the centreline, dominate this flow. Although the vortices are large and coherent and have a prevailing wavelength, λ_p, of approximately 10 cm, there is sufficient irregularity in their shape, size, and position to cause the spectrum of the induced fluctuation at the edge of the wake to be fairly broad (figure 13). The introduction of periodic forcing did not have a significant effect on the shape and scales of the large eddies visualized in this manner. For the unforced case, the flow-visualization results indicate that $\lambda_p/L_0 \sim 3$ for $Re_\theta = 600$. The theoretically most-amplified wave can be determined from figure 14 to have a frequency of 75 Hz corresponding to a wavelength of 9.9 cm for the higher velocity, $Re_\theta = 1035$, case. If one assumes that the normalized mean velocity profile is the same for both Reynolds number cases, the frequency of the most-amplified wave would scale with U_∞, and therefore, the wavelength remains constant as $\lambda = c/f \doteq U_\infty/f$. To determine L_0 for the $Re_\theta = 600$ case, we assumed L_0/θ is independent of Reynolds number in the turbulent range considered. Then, using the measured results for $Re_\theta = 1035$ (table 2), L_0 for the lower Reynolds number flow visualization case could be determined. The theoretical prediction for $Re_\theta = 600$ is $\lambda_p/L_0 = 3.5$, which is in good agreement with the flow-visualization results. Since the energy-containing eddies have a scale of the order of L_0 to $2L_0$, the wavelength of the most-amplified wave from linear stability theory is one to two times larger than the energy-containing scales of the turbulence.

The degree of two-dimensionality of these structures was first estimated by placing the smoke wire parallel to the circular cylinder but displacing it from the generator in the lateral direction in order that the smoke would not be entrained by the wake before $\bar{x} = 300$. The resulting photo (figure 24) indicates that the large eddies have a tendency to be two-dimensional, although the two-dimensionality is by no means perfect. There appears to be a variation of amplitudes along the span of the wake, as well as phase irregularities.

Coherence spectra calculated from u fluctuations sensed by two probes separated in the spanwise direction provide a quantitative measure of the two-dimensionality of the various scales. The two-point, cross-correlation function for stationary random variables $u_i(\boldsymbol{x}, t)$ and $u_j(\boldsymbol{x} + \boldsymbol{r}, t + \tau)$ is defined as

$$R_{ij}(\boldsymbol{x}, \boldsymbol{r}, \tau) = \overline{u_i(\boldsymbol{x}, t)\, u_j(\boldsymbol{x} + \boldsymbol{r}, t + \tau)}, \qquad (4.9)$$

and the cross-spectrum,

$$\phi_{ij}(\boldsymbol{x}, \boldsymbol{r}; f) = \frac{1}{2\pi} \int_{-\infty}^{\infty} R_{ij}(\boldsymbol{x}, \boldsymbol{r}; \tau)\, \mathrm{e}^{\mathrm{i}2\pi f\tau}\, \mathrm{d}\tau = C_{ij}(\boldsymbol{r}, \boldsymbol{x}; f) - \mathrm{i} Q_{ij}(\boldsymbol{x}, \boldsymbol{r}, f) \qquad (4.10)$$

$x \approx 600$　　　　　　　◀━━━━━ Flow ━━━━━　　　　　$x \approx 400$

FIGURE 24. The spanwise coherence of the large eddies in the wake of a circular cylinder at $\bar{x} \simeq 600$ and $Re_\theta = 600$.

where C_{ij} is called the cospectrum and Q_{ij}, the quadrature spectrum. The coherence spectrum is defined as

$$\mathrm{Coh}_{ij}(\boldsymbol{x}, \boldsymbol{r}; f) = \frac{C_{ij}^2(\boldsymbol{x}, \boldsymbol{r}; f) + Q_{ij}^2(\boldsymbol{x}, \boldsymbol{r}; f)}{F_{ii}(\boldsymbol{x}; f)\, F_{jj}(\boldsymbol{x} + \boldsymbol{r}; f)}, \tag{4.11}$$

where $F_{ii}(\boldsymbol{x}; f)$ and $F_{jj}(\boldsymbol{x} + \boldsymbol{r}; f)$ are the familiar (one-point) energy spectra, i.e.

$$\bar{u}_i^2(\boldsymbol{x}) = \int_{-\infty}^{\infty} F_{ii}(\boldsymbol{x}; f)\, \mathrm{d}f. \tag{4.12}$$

The phase angle θ_{ij} can be obtained as

$$\theta_{ij}(\boldsymbol{x}, \boldsymbol{r}; f) = \tan^{-1}\left[\frac{Q_{ij}}{C_{ij}}\right]. \tag{4.13}$$

The coherence spectrum is bounded, and its value must be between 0 and 1. We will consider the component $\mathrm{Coh}_{11}(\boldsymbol{x}, \Delta z; f)$, which represents the degree of spatial correlation between the Fourier components of $u_1(\boldsymbol{x}, t)$ and $u_1(\boldsymbol{x} + \boldsymbol{k}\Delta z, t + \tau)$ at the same frequency, where $\boldsymbol{k}$ is a unit vector in the z- or spanwise-direction.

A spanwise rake containing six hot-wire probes spaced from 1.1 to 2.54 cm apart was used for the coherence data. Measurements were taken in the wake of the flat plate, with and without excitation, at $\bar{x} = 430$ and 646, with the rake located at $\eta = 0$,
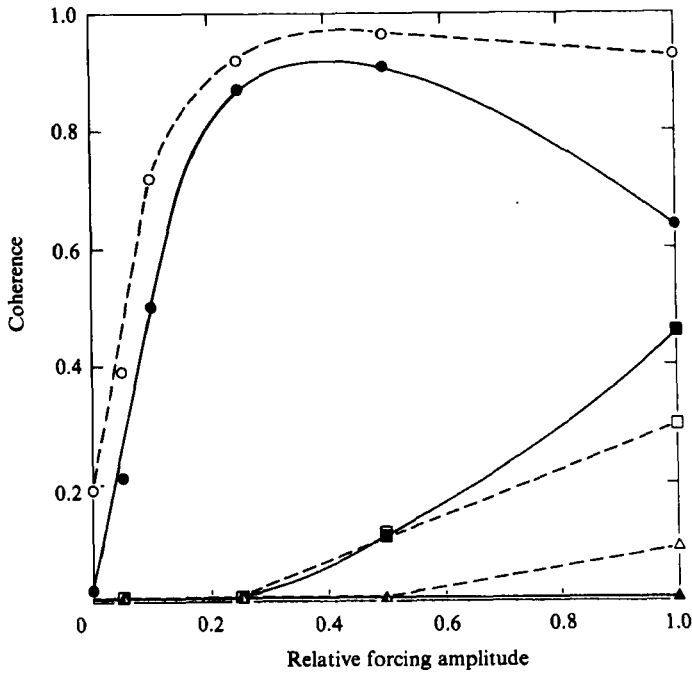
FIGURE 25. The response of the wake to various sinuous forcing levels. $\bar{x} = 646$ and $\eta = 0.6$. ●, $f = 50$ Hz, $\Delta z/L_0 = 10$; ○, $f = 50$ Hz, $\Delta z/L_0 = 0.4$; ■, $f = 100$ Hz, $\Delta z/L_0 = 10$; □, $f = 100$ Hz, $\Delta z/L_0 = 0.4$; ▲, $f = 150$ Hz, $\Delta z/L_0 = 10$; △, $f = 150$ Hz, $\Delta z/L_0 = 0.4$.
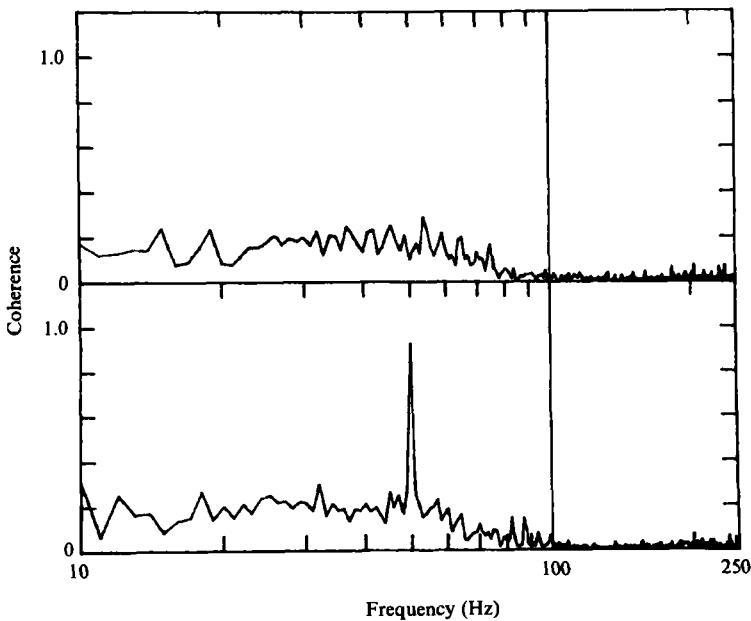

FIGURE 26. Coherence spectra measured at $\bar{x} = 646$, $\eta = 0.6$, and $\Delta z/L_0 = 0.4$ in the wake of the flat plate. Upper trace without forcing. Lower trace with forcing at 50 Hz.
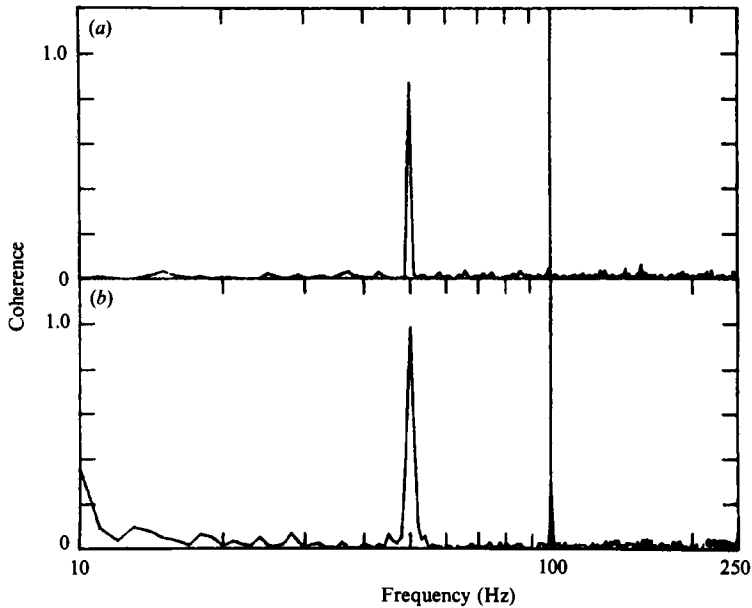
FIGURE 27. (a) Coherence spectrum measured at $\bar{x} = 646$, $\eta = 0.6$, and $\Delta z/L_0 = 10$, with forcing at 50 Hz. (b) Same as (a) except $\eta = 3$.

0.6, and 3. The lateral position $\eta = 0.6$ approximately corresponds to the location at which u-fluctuations are most energetic. The response of the wake at $\bar{x} = 646$ and $\eta = 0.6$ to various levels of excitation is shown in figure 25 for two Δz spacings, 1.1 and 25.4 cm apart. The values of the coherence at the excitation frequency (50.0 Hz) and its first and second harmonics as a function of amplitude are presented. All amplitudes are scaled by the highest amplitude of oscillation. Where the relative forcing amplitude was less than 0.25, the coherence spectrum responded in a linear manner. For amplitudes in the range of 0.25 to 0.5, the value of the coherence at the forcing frequency is nearly independent of Δz in the range investigated, at least up to $\Delta z/L_0 = 10$. The relative amount of energy tied up with the forcing frequency can be determined from the spectrum of the velocity fluctuations. In the case, the spectral peak at 50 Hz was one order of magnitude above the 'background' turbulent fluctuations.

Figure 26 shows the coherence spectra measured at $\bar{x} = 646$, $\eta = 0.6$, and $\Delta z/L_0 = 0.4$, with and without forcing. The forcing frequency was 50 Hz, corresponding to the expected predominant frequency at this $\bar{x}$, and the relative amplitude of forcing was 0.25. The effect of forcing sharply enhances the value of the coherence at the forcing frequency to 0.92, with little effect on the rest of the spectrum. The corresponding data for $\Delta z/L_0 = 10$ are shown in figure 27 (a), where only the data for the forced case are presented. The coherence for the unforced case at this separation vanished at all frequencies. For the forced case, the entire correlation is contained in the spectral spike at 50 Hz, for which the coherence is 0.87. Similar results were obtained at forcing levels as low as 0.05, where the peak correlation was 0.21 and 50 Hz. At $\eta = 3$ (figure 27b), a much higher coherence at the forcing frequency was measured (0.98), indicating that the large structure in the wake must be highly two-dimensional to generate such a result for the large spanwise separation, $\Delta z/L_0 = 10$. For the unforced case, the coherence is nearly zero from 10 to 260 Hz.
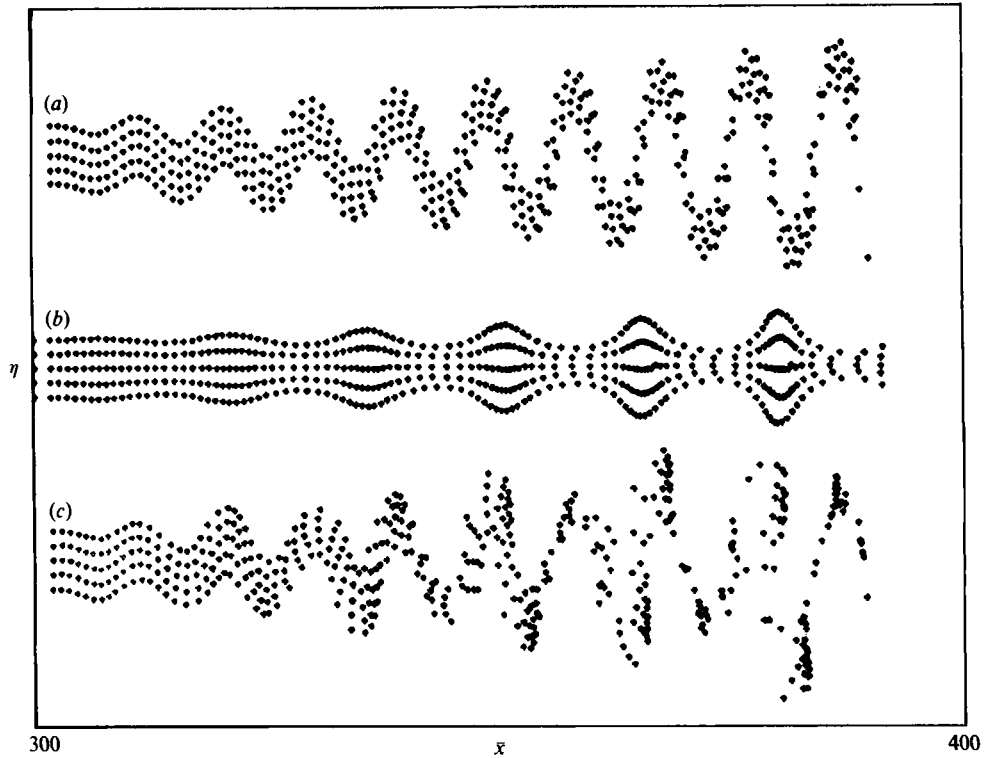
FIGURE 28. Streak-lines computed assuming spatial instability of parallel flow at $\bar{x} = 300$; (a) sinuous, most-amplified mode; (b) varicose, most-amplified mode; (c) combined modes.

The results indicate that a slight amount of forcing generates a strong two-dimensional wave in the wake at the forcing frequency.

Is the proposed model capable of explaining the large structures observed in figure 23? For this purpose, some streak-lines had to be calculated. Since the calculations were aimed at a qualitative understanding of this phenomenon, a parallel flow approximation was invoked locally. It was assumed that the particles were uniformly released at $\bar{x} = 300$, where $u_0/U_\infty = 0.06$. The prevailing wavelength from figure 23 was used to determine β corresponding to the spatially most-amplified sinuous wavetrain in this mean flow. Both u and v components of the perturbation velocity were calculated across the entire wake, and the corresponding particle paths were established from the equations

$$\frac{dx}{dt} = U[x(t), y(t), t]; \quad \frac{dy}{dt} = V[x(t), y(t), t]. \tag{4.14}$$

(For a detailed description of the procedure, see Michalke 1965.) The initial amplitude of the u-component of the velocity perturbations was $0.025\ U_\infty$. This corresponds to 30% of u_0, which is a constant in these calculations.

Five of the streak-lines calculated taking only the sinuous mode into consideration are shown in figure 28(a). The streak-lines have a sinusoidal pattern undulating about the centreline of the wake. The amplitude of the undulations increases with increasing distance from the source; at large distances, most of the particles congregate at the outer edge of the wake.
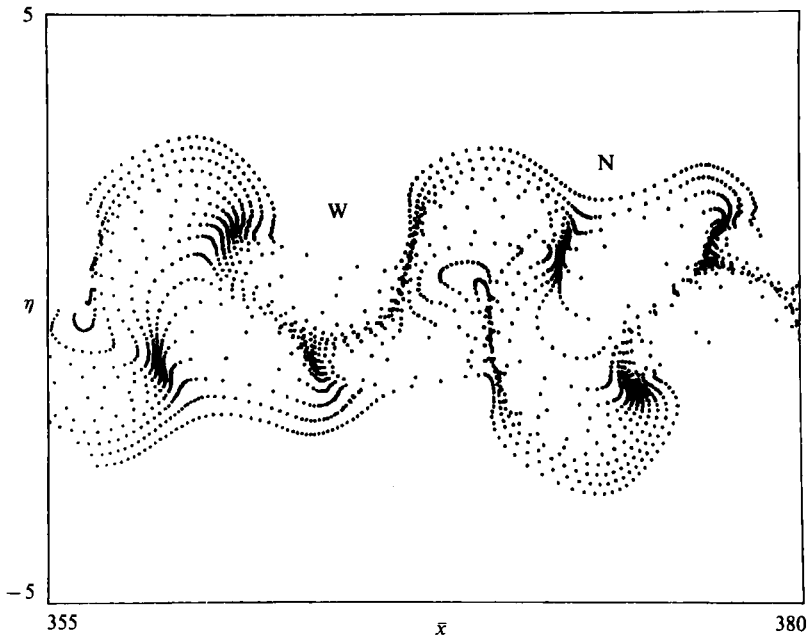
FIGURE 29. Streak-lines from figure 28(c) plotted on larger scale to show staggered nature of particle congregation.

The corresponding, most strongly amplified varicose mode has a perturbation frequency equal to $\frac{5}{8}$ of the frequency of the prevailing sinuous mode (not quite a subharmonic frequency). The computed streak-lines for the varicose mode are shown in figure 28(b). The particles in this figure congregate in lumps, which are symmetrical about the centreline of the wake. The streak-lines shown in figure 28(a) or (b) bear *no resemblance* to the observed coherent structures seen in figure 23.

The streak-lines shown in figure 28(c) represent the combined motion of both modes of instability when the coefficient of the velocity perturbation is still maintained at 0.025. The initial ratio between the amplitudes of u and v in the varicose mode and the sinuous mode was 0.7. (This number simply appeared because the eigenfunctions were not normalized; changing the initial ratio by a factor of two made no substantial difference in the pattern.) The initial phase relation between the modes was assumed to be zero. (Changing this number also had no effect on the basic pattern at some distance downstream from the source location.) The phase velocities of the two modes are not equal and differ by a few per cent.

The prevailing wavelength of the streak-lines (figure 28c) still corresponds to the prevailing wavelength of the sinuous mode, but the presence of the varicose mode not only modulates the streak-lines but also contributes to an apparent chaotic behaviour. Most important is the fact that these streak-lines, when replotted on a larger scale, resemble the pattern observed in the smoke photographs (figure 23). Namely, the particles congregate in a staggered manner about the centreline and the large eddies are, at times, separated by deep incursions of 'potential' fluid. Sometimes, these incursions are narrow (marked by the letter 'N' in figure 29) and, sometimes, they are wide (marked by 'W'). It therefore transpires that only the combination of both modes can successfully describe the flow.

The distributions of vorticity for the three cases considered in figure 28 were
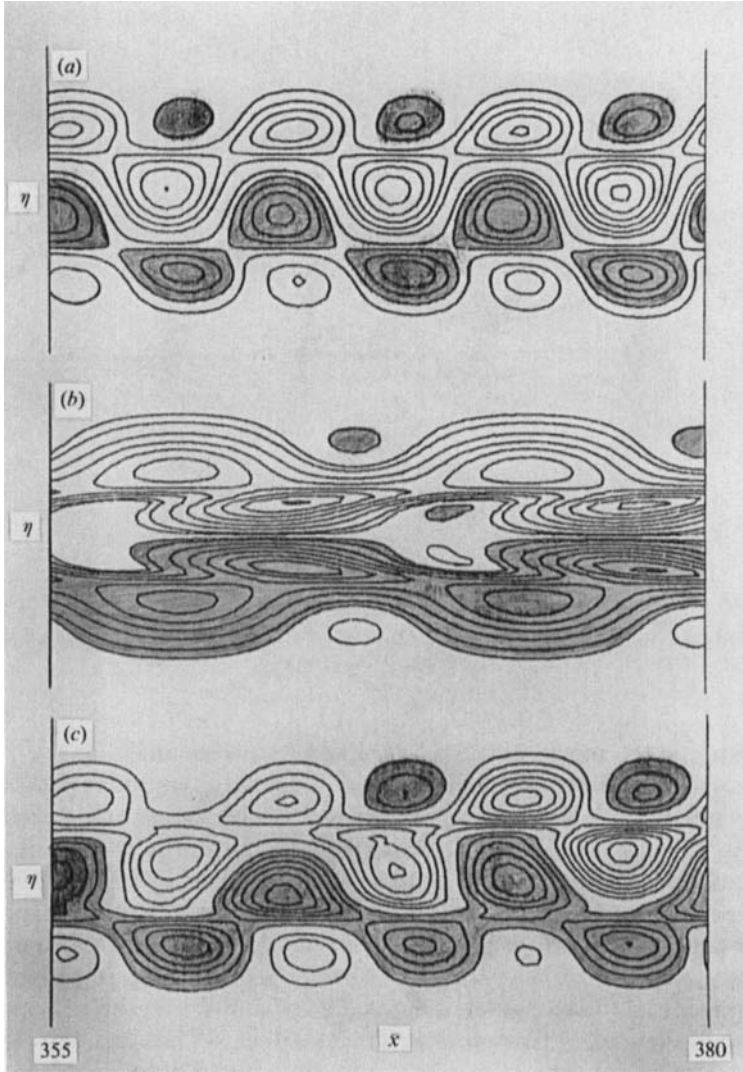
FIGURE 30. Vorticity perturbation contours computed for the three cases of streak-lines shown in figure 28: (a) sinuous, most-amplified mode; (b) varicose, most-amplified mode; (c) combined modes.

calculated directly from the eigenfunctions solved, because the vorticity perturbation

$$\omega(y) = -\frac{U''}{U - \beta/\alpha}\phi, \tag{4.15}$$

and the total vorticity

$$\Omega(x, y, t) = -U' + 0.015\,\mathrm{RP}\,\{\omega(y)\exp\left[\mathrm{i}(\alpha x - \beta t)\right]\}, \tag{4.16}$$

which is, of course, periodic in time. The vorticity contours plotted in figure 30 were calculated for $t = 2\pi/\beta$ and for $355 \leqslant \bar{x} \leqslant 385$, as in figure 29. (The shaded regions

correspond to negative vorticity.) By neglecting either the varicose mode [figure 30a] or the sinuous mode [figure 30b], the resulting vorticity contours appear to be very regular. The contours are either symmetrical or antisymmetrical about the centreline and indicate intensification of vorticity with increasing $\bar{x}$. The vorticity contours resulting from the combined two modes of instability [figure 30c] are surprisingly similar to the contours produced by the sinuous mode alone. One may notice, however, that the intensity of the contours in figure 30c are modulated by the varicose mode, even if they are not severely distorted by the addition of this mode. A simple superposition of figure 30c on figure 28 leads to the conclusion that a congregation of particles observed in a *still photograph* does not necessarily correspond to a concentration of vorticity.

5. Discussion

The velocity and length scales in a plane, turbulent, and supposedly self-preserving wake are dependent on inflow conditions and, therefore, on the shape and size of the obstacle generating the wake. We could not prove that these scales will not become universal functions of (x/θ) at extremely large values of (x/θ), but the distances at which this may (or may not) occur may be so large as to have no practical impact on the problem. The range of x/θ values in the present study extended up to 2000, corresponding to $u_0/U \sim 0.03$. The dependence of the plane mixing layer on inflow conditions was observed some years ago (Champagne, Pao & Wygnanski, 1976) and traced to the presence of large coherent structures (Oster & Wygnanski 1982). The existence of large coherent structures in a wake, however, was often confused with vortex shedding, which was so ably discussed by Karman (1912) in the lee of a circular cylinder at low Reynolds numbers. The large eddies proposed by Townsend (1956) and Grant (1958) bear little resemblance to the structures observed presently, although Townsend suggested that the large eddies present in fully turbulent free shear flows might have been generated by hydrodynamic instability of the mean flow.

What is the cause for the apparent dependence of the small-deficit wake on the shape of the generator? The nature of the flow in the vicinity of the generator, including any vortices shed by the generator, can provide a plausible explanation for this phenomenon. The frequency, amplitude, and the predominant mode of the initial perturbation vary from one geometry to another. For all geometries investigated, the *predominant* mode of shedding was sinuous, but the presence of the varicose mode was also detected in the vicinity of the low-solidity screens and circular cylinder. The strongest sinuous oscillations were observed downstream of the thick symmetrical airfoil because the initiation of separation from one surface changed the circulation around the airfoil, moving the front stagnation point toward the separated surface and therefore initiating a separation from the opposite surface. The amplitude at the shedding frequency was three orders of magnitude stronger than the background turbulence. The amplitudes of the oscillations generated by a circular cylinder and by the screens were approximately two orders of magnitude above the background, while the amplitude of the oscillations downstream of the solid strip held normal to the flow was of the same order of magnitude as the background.

It is also suspected that the lower the frequency of the shedding, the more persistent the initial effects will be; in fact, the frequency of shedding downstream of the symmetrical airfoil of a given thickness depends on the chord length, provided the flow separates upstream of the trailing edge. The effects of frequency, however, appear to be less significant than the effects of amplitude. A detailed investigation
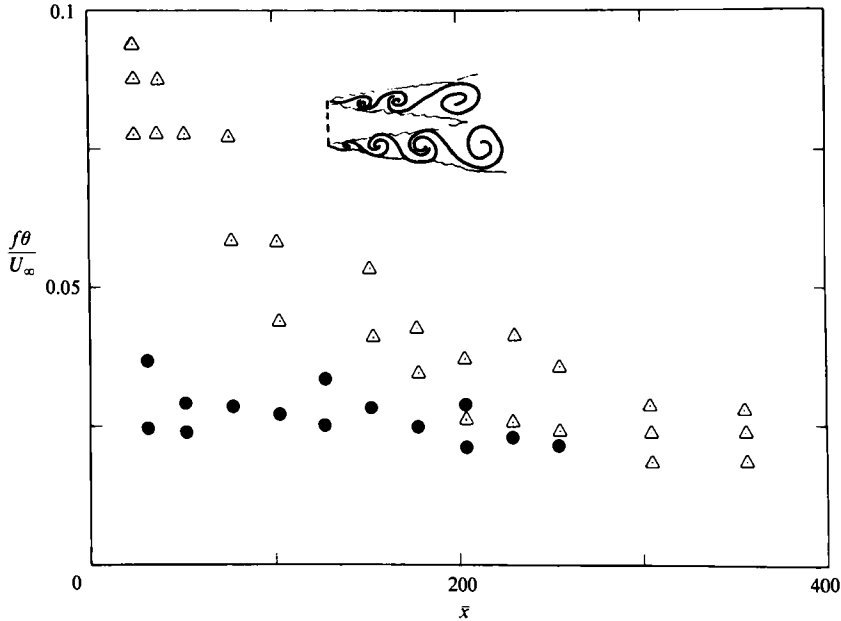
FIGURE 31. The measured predominant frequencies in the wake of: (a) ●, a circular $\frac{3}{16}$ in. cylinder, $Re_\theta = 2000$; (b) △, the 30 % solidity screen, $Re_\theta = 2000$.

of the near wake has been undertaken in order to determine the effects of inflow condition more precisely.

Cimbala *et al.* (1981) observed, with the aid of a smoke wire, the evolution of large coherent structures in a wake of a circular cylinder up to $Re_d < 2000$ and in a wake of two screens at comparable Re. These structures became apparent some 200 diameters downstream of the cylinder and had a regular frequency two to three times lower than the Strouhal frequency. They were unable, however, to corroborate their results with spectral measurements for their high-Reynolds-number case and attributed it to the high turbulence level in their tunnel. Some measurements of spectra at the outer edge of the wake were carried out for two wake generators: (i) a circular cylinder at $Re_\theta = 2500$ corresponding to $Re_d = 5000$ and (ii) a screen having 45 % solidity, also at $Re_\theta = 2500$. In the immediate neighbourhood of the cylinder, the predominant spectral peak (not shown) corresponded to the shedding frequency of the cylinder, i.e. at $St_d = 0.206$ or $St_\theta = 0.10$. At $\bar{x} > 50$, the predominant spectral peak dropped quite abruptly to $St_\theta \simeq 0.03$. Thereafter, the evolution of the spectral peak was rather slow and is hardly detectable on the scale shown in figure 31. The spectral peaks associated with the screen tailored to produce the same momentum thickness as the circular cylinder are similar to those mentioned above at $\bar{x} > 250$. The big difference between the two flows occurs at $50 < \bar{x} < 250$, where the characteristic frequency of the spectral peaks generated by the screen decreases slowly with $\bar{x}$. At $\bar{x} > 150$, one may detect the appearance of an additional peak in the spectrum, which roughly corresponds to the spectral peak in the far wake of the circular cylinder; this peak amplifies quickly and dominates the spectrum at $\bar{x} > 200$. It seems that the coherent structures in the near wake of this particular screen retain some of their characteristics up to $\bar{x} = 250$, while in the wake of the circular cylinder, this transition is accomplished at $\bar{x} = 50$. It is believed that the shear layers generated in the wake of the screen (see insert in figure 31) undergo an instability process

reminiscent of the plane mixing layer (Gaster *et al.* 1985), generating eddies whose characteristic frequency decreases in the direction of streaming. Whether these eddies grow by entraining fluid from the surrounding stream or by a process of amalgamation remains to be seen.

Since Cimbala *et al.* (1981) did not observe any vortex amalgamation in their visualization experiments, one would be inclined to think that the gradual decrease in the characteristic frequency stemming from an increase in the wavelength of these eddies is caused by entrainment. In any event, once the scale of these eddies becomes comparable to the width of the screen, an interaction between two shear layers of opposing vorticity has to occur before the wake will become 'fully developed'. It is possible that a phase accommodation ensues, resulting in a slow evolution of the typical large structures existing in the self-preserving region. The evolution of the fully developed wake is currently being investigated, but the importance of initial conditions is evident in figure 31.

The mutual interaction between the large coherent structures and the mean flow is outside the scope of the linear stability theory. However, the dependence of the mean flow field on the initial conditions, and consequently on the large coherent structures, poses precisely such a problem. The notion that the free-stream turbulence and the shape of the generator may have an effect on the development of a self-preserving wake was proposed by Symes & Fink (1977). These authors observed that the wake generated by a rectangular cylinder did not evolve in the same manner as the wake generated by a circular cylinder, but the most important observation stems from the fact that the evolution of the wake was sensitive to grid turbulence, whose integral scale was an order of magnitude larger than the scale of the generator. This suggested that the externally imposed turbulence interacted with the flow far downstream, where the typical scales in the wake and in the free stream became comparable. It also implied that an instability mechanism might be responsible for this result. The present investigation confirmed this notion, although nonlinear terms have to be considered in order to assess the interaction between the mean flow and the imposed oscillation. Perhaps, an integral approach similar to the one used by Ko, Kubota & Lees (1970) might predict such an interaction through the Reynolds stress. The concept of flow equilibrium and self-preservation has to be carefully reconsidered in view of the present findings, in spite of the fact that the normalized shape of the mean velocity profile was not affected. The dependence of the lateral distribution of the turbulent intensities on the nature of the generator (figure 7) and the relatively poor collapse of the dimensionless data onto a single function for a given wake generator raise the possibility that the flow is not in equilibrium. Although this possibility was considered remote at the start of this investigation, a plot showing the difference between the maximum intensity $(\bar{u}^2)_{max}$ and the intensity on the centreline of the wake $(\bar{u}^2)_{CL}$ normalized by u_0^2 is shown in figure 32 for the wake of the flat plate. If the flow was in perfect equilibrium, then $(\bar{u}^2)_{max} - (\bar{u}^2)_{CL}/u_0^2$ should have been constant at all $\bar{x}$. Although this plot is very susceptible to experimental inaccuracies and should be treated with due caution, the lack of constancy might have been caused by a nonlinear interaction between the varicose mode and the sinuous mode of instability. The possible interaction between the two modes will be investigated in detail by forcing the wake simultaneously with a combination of modes.

The assumption of parallel flow (3.2) makes the eigenfunction $\phi(y)$ and the eigenvalues α and β invariant with respect to streamwise distance from the generator. Thus, for $\beta = 0$ (i.e. spatially amplified waves), only a single mode containing the
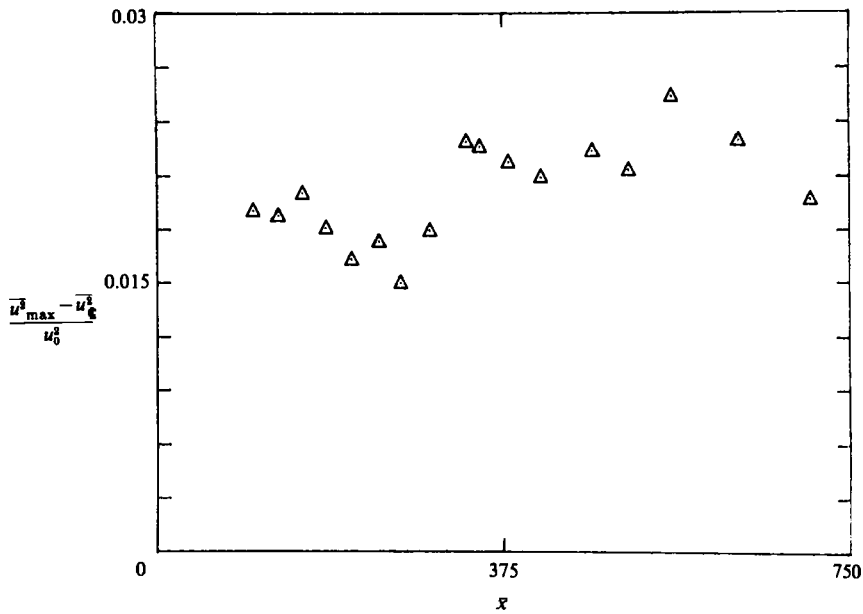
FIGURE 32. The variation of turbulent intensity defect on the centreline of the wake of a flat plate.

largest $|-\alpha_i|$ need be considered. However, the amplification rates in the small-deficit, plane wake are so small that one cannot disregard one mode of instability in favour of another simply because its $|-\alpha_i|$ is the largest. The long distances required for an unstable wave to amplify increase the relative significance of the longitudinal gradients in the mean velocity. By neglecting the varicose mode in favour of the sinuous one, Sato & Kuriki (1961) had to resort to nonlinear effects in their attempt to explain the cause for the generation of two rows of vortices. Mattingly & Criminale (1972) offered an alternate explanation, which is based on the vorticity distribution of the sinuous mode being superposed on the mean vorticity. The generation of a vortex structure reminiscent of a Karman vortex street can quite easily be attributed to the superposition of the two instability modes, keeping in mind that the most unstable frequency of the varicose mode is only slightly higher than a subharmonic of the most unstable sinuous mode. Sinuous forcing of the flow has little effect on the shape of the large eddies visualized by smoke until the amplitude of the forcing becomes high. In this case, the smoke pattern is more regular and the eddies are located closer to the centreline than in the corresponding unforced wake.

6. Conclusions

It was experimentally observed that the characteristic velocity and length scales, u_0 and L_0, when suitably scaled by the momentum thickness and the free-stream velocity, do not exhibit universal behaviour and do depend on the inflow conditions and therefore on the geometry of the wake generator. The mean velocity profiles for each wake, when normalized by their own velocity and length scales, are self-preserving and are also identical for all wake generators. The distributions of the turbulence intensities normalized in the same manner are almost self-preserving, but they are dependent on the geometry of the wake generator.

Linear inviscid stability theory, in which the divergence of the mean flow was taken into account, predicts quite well the amplification and the transverse distributions of amplitudes and phases of externally imposed sinuous waves in a fully developed turbulent wake generated by a flat plate. It appears that the large, coherent, vortex structures occurring naturally in a wake can be modelled to some extent by linear stability theory. Furthermore, the interaction of the two possible modes of instability may be responsible for the apparent Karman vortex street-type of structures observed visually in the small-deficit, turbulent wake.

REFERENCES

BOUTHIER, M. 1972 *J. Méc.* 11, 599.

BROWN, G. L. & ROSHKO, A. 1974 *J. Fluid Mech.* 64, 775.

CHAMPAGNE, F. H. 1978 *J. Fluid Mech.* 86, 67.

CHAMPAGNE, F. H., PAO, Y. H. & WYGNANSKI, I. J. 1976 *J. Fluid Mech.* 74, 209.

CIMBALA, J., NAGIB, H. & ROSHKO, A. 1981 *Bull. Am. Phys. Soc.* Ser. 11, 2.

CRIGHTON, D. G. & GASTER, M. 1976 *J. Fluid Mech.* 77, 297.

FREYMUTH, P. 1966 *J. Fluid Mech.* 25, 683.

GASTER, M., KIT, E. & WYGNANSKI, I. 1985 *J. Fluid Mech.* 150, 23.

GRANT, H. L. 1958 *J. Fluid Mech.* 4, 149.

KARMAN, TH. V. 1912 *Nachr. Ges. Wiss. Göttingen* 547.

KO, D. R. S., KUBOTA, T. & LEES, L. 1970 *J. Fluid Mech.* 40, 315.

MARASLI, B. 1983 Master's thesis, AME Dept., University of Arizona.

MATTINGLY, G. E. & CRIMINALE, W. O. 1972 *J. Fluid Mech.* 51, 233.

MICHALKE, A. 1965 *J. Fluid Mech.* 23, 521.

NARASIMHA, R. & PRABHU, A. 1972 *J. Fluid Mech.* 54, 1.

OSTER, D. & WYGNANSKI, I. 1982 *J. Fluid Mech.* 123, 91.

SATO, H. & KURIKI, K. 1961 *J. Fluid Mech.* 11, 321.

SREENIVASAN, K. R. 1981 *AIAA J.* 19, 1365.

SREENIVASAN, K. R. & NARASIMHA, R. 1982 *Trans. ASME J. Fluids Engng* 104, 167.

STRANGE, P. J. R. 1982 Ph.D. thesis, University of Leeds.

SYMES, C. R. & FINK, L. E. 1977 In *Structures and Mechanisms of Turbulence I*, proceedings. p. 86, Berlin.

TOWNSEND, A. A. 1947 *Proc. R. Soc. Lond.* A190, 551.

TOWNSEND, A. A. 1949 *Austral. J. Sci.* 2, 451.

TOWNSEND, A. A. 1956 *The Structure of Turbulent Shear Flow*. Cambridge University Press.

TOWNSEND, A. A. 1970 *The Structure of Turbulent Shear Flow*, 2nd edn. Cambridge University Press.

UBEROI, M. S. & FREYMUTH, P. 1969 *Phys. Fluids* 12, 1359.

WYGNANSKI, I., OSTER, D. & FIEDLER, H. 1979 In *Proc. 2nd Symp. on Turbulent Shear Flows*. London.

YAMADA, H., KAWATA, Y., OSAKA, H. & KAGEYAMA, Y. 1980 Tech. Rep. Yamaguchi University, Japan, vol. 2, no. 4.

ZABUSKI, N. J. & DEEM, G. S. 1971 *J. Fluid Mech.* 47, 353.